

1           **OBSERVATIONS OF HIGHLY OXIDISED**  
2           **MOLECULES AND PARTICLE NUCLEATION**  
3           **IN THE ATMOSPHERE OF BEIJING**

4  
5           **James Brean<sup>1</sup>, Roy M. Harrison<sup>1\*†</sup>, Zongbo Shi<sup>1</sup>**  
6           **David C.S. Beddows<sup>1</sup>, W. Joe F. Acton<sup>2</sup>**  
7           **C. Nicholas Hewitt<sup>2</sup>, Freya A. Squires<sup>3</sup> and James Lee<sup>3</sup>**  
8  
9

10           <sup>1</sup>**Division of Environmental Health and Risk Management,**  
11           **School of Geography, Earth and Environmental Sciences**  
12           **University of Birmingham**  
13           **Edgbaston, Birmingham B15 2TT**  
14           **United Kingdom**

15  
16           <sup>2</sup>**Lancaster Environment Centre**  
17           **Lancaster University, Lancaster LA1 4YQ**  
18           **United Kingdom**

19  
20           <sup>3</sup>**National Centre for Atmospheric Science**  
21           **Wolfson Atmospheric Chemistry Laboratory**  
22           **University of York, York YO10 5DD**  
23           **United Kingdom**  
24

---

\* To whom correspondence should be addressed.  
Tele: +44 121 414 3494; Fax: +44 121 414 3709; Email: r.m.harrison@bham.ac.uk

†Also at: Department of Environmental Sciences / Center of Excellence in Environmental Studies, King Abdulaziz University, PO Box 80203, Jeddah, 21589, Saudi Arabia

25 **ABSTRACT**

26 Particle nucleation is one of the main sources of atmospheric particulate matter by number, with new  
27 particles having great relevance for human health and climate. Highly oxidised multifunctional  
28 organic molecules (HOMs) have been recently identified as key constituents in the growth, and,  
29 sometimes, in initial formation of new particles. While there have been many studies of HOMs in  
30 atmospheric chambers, flow tubes and clean environments, analyses of data from polluted  
31 environments are scarce. Here, measurements of HOMs and particle size distributions down to small  
32 molecular clusters are presented alongside volatile organic compounds (VOC) and trace gas data from  
33 a campaign in June 2017, in Beijing. Many gas phase HOMs have been characterised and their  
34 temporal trends and behaviours analysed in the context of new particle formation. The HOMs  
35 identified have a comparable degree of oxidation to those seen in other, cleaner, environments, likely  
36 due to an interplay between the higher temperatures facilitating rapid hydrogen abstractions and the  
37 higher concentrations of  $\text{NO}_x$  and other  $\text{RO}_2\cdot$  terminators ending the autoxidation sequence more  
38 rapidly. Our data indicate that alkylbenzenes, monoterpenes, and isoprene are important precursor  
39 VOCs for HOMs in Beijing. Many of the  $\text{C}_5$  and  $\text{C}_{10}$  compounds derived from isoprene and  
40 monoterpenes have a slightly greater degree of average oxidation state of carbon compared to those  
41 from other precursors. Most HOMs except for large dimers have daytime peak concentrations,  
42 indicating the importance of  $\text{OH}\cdot$  chemistry in the formation of HOMs, as  $\text{O}_3$  tends to be lower on  
43 days with higher HOM concentrations ; similarly, VOC concentrations are lower on the days with  
44 higher HOM concentrations. The daytime peaks of HOMs coincide with the growth of freshly formed  
45 new particles, and their initial formation coincides with the peak in sulfuric acid vapours, suggesting  
46 that the nucleation process is sulfuric acid-dependent, with HOMs contributing to subsequent particle  
47 growth.

48

49

## 50 1. INTRODUCTION

51 Atmospheric particle nucleation, or the formation of solid or liquid particles from vapour phase  
52 precursors is one of the dominant sources of global aerosol by number, with primary emissions  
53 typically dominating the mass loadings (Tomasi et al., 2016). New particle formation (NPF) or the  
54 secondary formation of fresh particles is a two-step process comprising of initial homogeneous  
55 nucleation of thermodynamically stable clusters and their subsequent growth. The rate of growth  
56 needs be fast enough to out-compete the loss of these particles by coagulation and condensation  
57 processes in order for the new particles to grow, and hence NPF is a function of the competition  
58 between source and sink (Gong et al., 2010). New particle formation has been shown to occur  
59 across a wide range of environments (Kulmala et al., 2005). The high particle load in urban  
60 environments was thought to suppress new particle formation until measurements in the early 2000s  
61 (McMurry et al., 2000; Shi et al., 2001; Alam et al., 2003), with frequent occurrences observed even  
62 in the most polluted urban centres. NPF events in Beijing occur on about 40% of days annually,  
63 with the highest rates in the spring (Wu et al., 2007, 2008; Wang et al., 2016). Chu et al. (2019)  
64 review many studies of NPF which have taken place in China and highlight the need for long-term  
65 observations and mechanistic studies.

66

67 NPF can lead to production of cloud condensation nuclei (CCN) (Wiedensohler et al., 2009; Yu and  
68 Luo, 2009; Yue et al., 2011; Kerminen et al., 2012) which influences the radiative atmospheric  
69 forcing (Penner et al., 2011). A high particle count, such as that caused by nucleation events, has  
70 been shown to precede haze events in environments such as Beijing (Guo et al., 2014). These events  
71 are detrimental to health and quality of life. The sub-100 nm fraction of particles to which new  
72 particle formation contributes to is often referred to as the ultrafine fraction. Ultrafine particles  
73 (UFPs) pose risks to human health due to their high number concentration. UFPs exhibit gas-like  
74 behaviour and enter all parts of the lung before penetrating into the bloodstream (Miller et al.,  
75 2017). They can initiate inflammation via oxidative stress responses, progressing conditions such as

76 atherosclerosis and initiating cardiovascular responses such as hypertension through to myocardial  
77 infarction (Delfino et al., 2005; Brook et al., 2010).

78

79 Highly oxidised multifunctional molecules (HOMs), organic molecules with O:C ratios >0.6, are  
80 the result of atmospheric autoxidation and have recently been subject to much investigation, in part  
81 because the extremely low volatilities arising from their high O:C ratios favour their condensation  
82 into the particulate phase. HOMs are most well characterised as the product of oxidation of the  
83 biogenic monoterpene compound  $\alpha$ -pinene (Riccobono et al., 2014; Tröstl et al., 2016; Bianchi et  
84 al., 2017). Although globally, biogenic volatile organic compound (BVOC) concentrations far  
85 exceed anthropogenic volatile organic compound (AVOC) concentrations, in the urban environment  
86 the anthropogenic fraction is far more significant. Formation of HOMs from aromatic compounds  
87 has been demonstrated in laboratory studies and these have been hypothesised to be large drivers of  
88 NPF in urban environments (Wang et al., 2017; Molteni et al., 2018; Qi et al., 2018). The formation  
89 of HOMs through autoxidation processes begins with the reaction of VOCs with OH, O<sub>3</sub> or NO<sub>3</sub>;  
90 formation of a peroxy radical (RO<sub>2</sub>) is followed by rapid O<sub>2</sub> additions and intra-molecular hydrogen  
91 abstractions (Jokinen et al., 2014; Rissanen et al., 2014; Kurtén et al., 2015). Furthermore,  
92 generation of oligomers from stabilised Criegee intermediates arising from short chain alkenes has  
93 been hypothesised as a contributor of Extremely Low Volatility Organic Compounds (ELVOCs)  
94 and Low Volatility Organic Compounds (LVOCs) (Zhao et al., 2015). The low volatilities of these  
95 molecules arise from their numerous oxygen-containing functionalities, and this allows them to  
96 make a significant contribution to early stage particle growth where other species cannot due to the  
97 Kelvin effect (Tröstl et al., 2016), although the contribution of HOMs to the initial molecular  
98 clusters is still debated (Kurtén et al., 2016; Elm et al., 2017; Myllys et al., 2017).

99

100 Recent technological advances have facilitated insights into the very first steps of nucleation which  
101 were previously unseen, with mass spectrometric techniques such as the Atmospheric Pressure

102 Interface Time of Flight Mass Spectrometer (APi-ToF) and its chemical ionisation counterpart (CI-  
103 APi-ToF) allowing for high mass and time resolution measurements of low volatility compounds  
104 and molecular clusters. Diethylene glycol based particle counters, such as the Particle Size  
105 Magnifier (PSM) allow for measurements of particle size distributions down to the smallest  
106 molecular clusters nearing 1 nm. Recent chamber studies have elucidated the contribution of  
107 individual species to particle nucleation, ammonia and amines greatly enhancing the rate of sulfuric  
108 acid nucleation (Kirkby et al., 2011; Almeida et al., 2013). In these studies, HOMs have been  
109 identified, formed through autoxidation mechanisms (Schobesberger et al., 2013; Riccobono et al.,  
110 2014; Ehn et al., 2014). These are key to early particle growth (Tröstl et al., 2016) and can nucleate  
111 even in the absence of sulfuric acid in chambers (Kirkby et al., 2016) and in the free troposphere  
112 (Rose et al., 2018). In this paper, we report the results of HOM and particle size measurements  
113 during a summer campaign in Beijing, China.

114

## 115 **2. DATA AND METHODS**

### 116 **2.1. Sampling Site**

117 Sampling was performed as part of the Air Pollution and Human Health in a Developing Megacity  
118 (APHH-Beijing) campaign, a large international collaborative project examining emissions,  
119 processes and health effects of air pollution. For a comprehensive overview of the programme, see  
120 Shi et al. (2019). All sampling was conducted across a one month period at the Institute for  
121 Atmospheric Physics (IAP), Chinese Academy of Sciences, Beijing (39°58.53'N, 116°22.69'E).

122 The sampling was conducted from a shipping container, with sampling inlets 1-2 metres above  
123 ground level, the nearest road being 30 metres away. Meteorological parameters (wind speed, wind  
124 direction, relative humidity (RH) and temperature) were measured at the IAP meteorological tower,  
125 20 metres away from the sampling site, 30 metres from the nearest road at a height of 120 metres.

126 Data was continuously taken from the CI-API-ToF during a two week period, but due to data losses

127 only five days of data is presented here. Particle size distribution measurements were taken during a  
128 33 day period from 24/05/2017 – 26/06/2017.

129

## 130 **2.2 Chemical Ionisation Atmospheric Pressure Interface Time of Flight Mass** 131 **Spectrometry**

132 The Aerodyne Nitrate Chemical Ionisation Atmospheric Pressure Interface Time of Flight Mass  
133 Spectrometer (CI-APi-ToF) was used to make measurements of neutral oxidised organic  
134 compounds, sulfuric acid and their molecular clusters at high time resolution with high resolving  
135 power. The ionization system charges molecules by adduct formation, such as in the case of organic  
136 compounds with two or more hydrogen bond donor groups (Hytinen et al., 2015), or proton  
137 transfer in the case of strong acids like sulfuric acid. Hydroxyl or hydroperoxyl functionalities are  
138 both common hydrogen bond donating groups, with hydroperoxyl being the more efficient  
139 hydrogen bond donor (Møller et al., 2017). This instrument has been explained in great detail  
140 elsewhere (Junninen et al., 2010; Jokinen et al., 2012), but briefly the front end consists of a  
141 chemical ionisation system where a 10 LPM sample flow is drawn in through the 1 metre length 1”  
142 OD stainless steel tubing opening. A secondary flow was run parallel and concentric to this sample  
143 flow, rendering the reaction chamber effectively wall-less. A 3 SCCM flow of a carrier gas (N<sub>2</sub>) is  
144 passed over a reservoir of liquid HNO<sub>3</sub>, entraining vapour which is subsequently ionised to NO<sub>3</sub><sup>-</sup> via  
145 an X-ray source. This flow is then guided into the sample flow. . The nitrate ions will then charge  
146 molecules either by clustering or proton transfer. The mixed flows travelling at 10 LPM enter the  
147 critical orifice at the front end of the instrument at 0.8 LPM and are guided through a series of  
148 differentially pumped chambers before reaching the ToF analyser. Two of these chambers contain  
149 quadrupoles which can be used to select greater sensitivity for certain mass ranges, and the voltages  
150 across each individual chamber can be tuned to maximise sensitivity and resolution for ions of  
151 interest. Mass spectra are taken at a frequency of 20 kHz but are recorded at a rate of 1 Hz. All data  
152 analysis was carried out in the *Tofware* package in *Igor Pro 6* (Tofwerk AG, Switzerland). A seven

153 point mass calibration was performed for every minute of data, and all data was normalised to  
154 signal at 62, 80 and 125  $m/Q$  to account for fluctuations in ion signal, these masses representing  
155  $\text{NO}_3^-$ ,  $\text{H}_2\text{ONO}_3^-$  and  $\text{HNO}_3\text{NO}_3^-$  respectively. The resultant normalised counts have been multiplied  
156 by  $10^5$  so magnitudes are similar to the original count rates. Typical values for calibration  
157 coefficients range from  $10^9$ - $10^{10}$  molecules  $\text{cm}^{-3}$  from these normalised data (Kürten et al., 2012),  
158 producing peak sulfuric acid concentrations in the range of  $10^6$  molecules  $\text{cm}^{-3}$ . From the very  
159 limited periods with simultaneous data for  $\text{SO}_2$ , OH radical and condensation sink, it was possible  
160 to calculate  $\text{H}_2\text{SO}_4$  concentrations of  $10^3$  to  $10^5$  molec  $\text{cm}^{-3}$ , in which range the calibration constant  
161 was  $7.0 \pm 1.6 \times 10^8 \text{ cm}^{-3}$  which fits well with that expected for this concentration range (Kürten et  
162 al., 2012). The nitrate-water cluster is included as the presence of many nitrate-water clusters of the  
163 general formula  $(\text{H}_2\text{O})_x(\text{HNO}_3)_y\text{NO}_3^-$  were found, where  $x = (1, 2, 3... 20)$  and  $y = (0, 1)$ . No  
164 sensitivity calibration was performed for these measurements, and so all values are reported in  
165 normalised signal intensity. Due to the high resolving power of the CI-APi-ToF system (mass  
166 resolution of 3500  $m/\text{dm}$  and mass accuracy of 20 ppm at 288  $m/Q$ ), multiple peaks can be fit at the  
167 same unit mass and their molecular formulae assigned. These peaks follow the general formula  
168  $\text{C}_x\text{H}_y\text{O}_z\text{N}_w$  where  $x = 2-20$ ,  $y = 2-32$ ,  $z = 4-16$  and  $w = 0-2$ , spanning from small organic acids like  
169 oxalic and malonic acid through to large dimers of oxidised monoterpene  $\text{RO}_2$  radicals such as  
170  $\text{C}_{20}\text{H}_{31}\text{O}_9\text{N}$ . Beyond 500  $m/Q$ , peak fitting and assignment of compositions becomes problematic as  
171 signal decreases, mass accuracy decreases, and the total number of chemical compositions  
172 increases, so peaks above the  $\text{C}_{20}$  region have not been assigned, and a number of peaks have been  
173 unassigned due to this uncertainty (Cubison and Jimenez, 2015). As proton transfer mostly happens  
174 with acids, and nearly all HOM molecules will be charged by adduct formation it is possible to infer  
175 the uncharged formula; therefore all HOMs from here onwards will be listed as their uncharged  
176 form.

177

178

### 179 **2.3. Size Distribution Measurements**

180 Two Scanning Mobility Particle Sizer (SMPS) instruments measured particle size distributions at  
181 15 minute time resolution, one LongSMPS (TSI 3080 EC, 3082 Long DMA, 3775 CPC, TSI, USA)  
182 and one NanoSMPS (3082 EC, 3082 Nano DMA, 3776 CPC, TSI, USA) measuring the ranges 14-  
183 615 nm and 4-65 nm respectively. A Particle Size Magnifier (A10, Airmodus, FN) linked to a CPC  
184 (3775, TSI, USA) measured the sub-3 nm size fraction. The PSM was run in stepping mode,  
185 operating at four different saturator flows to vary the lowest size cut-off of particles that it will grow  
186 (this cut-off is technically a point of 50% detection efficiency) of <1.30, 1.36, 1.67 and 2.01 nm.  
187 The instrument switched between saturator flows per 2.5 minutes, giving a sub-2.01 nm size  
188 distribution every 10 minutes. The data was treated with a moving average filter to account for  
189 jumps in total particle count, and due to the similar behaviour of the two upper and two lower size  
190 cuts, these have been averaged to two size cuts at 1.30 and 1.84 nm.

191

### 192 **2.4. Calculations**

193 The condensation sink (CS) was calculated from the size distribution data as follows:

$$194 \quad CS = 4\pi D \sum_{d'_p} \beta_{m,d'_p} d'_p N_{d'_p} \quad (1)$$

195

196 where D is the diffusion coefficient of the diffusing vapour (assumed sulfuric acid),  $\beta_m$  is a  
197 transition regime correction (Kulmala et al., 2012),  $d'_p$  is particle diameter, and  $N_{d'_p}$  is the number  
198 of particles at diameter  $d'_p$ .

199

### 200 **2.5. Other Measurements**

201 Measurements of the classical air pollutants were measured on the same site, and have been  
202 reported in the campaign overview paper (Shi et al., 2019). SO<sub>2</sub> was measured using a 43i SO<sub>2</sub>  
203 analyser (ThermoFisher Scientific, USA), O<sub>3</sub> with a 49i O<sub>3</sub> analyser (ThermoFisher Scientific,



204 USA) and NO<sub>x</sub> with a 42i-TL Trace NO<sub>x</sub> analyser (ThermoFisher Scientific, USA), and a T500U  
205 CAPS NO<sub>2</sub> analyser (Teledyne API, USA). VOC mixing ratios were measured using a Proton  
206 Transfer Reaction-Time of Flight-Mass Spectrometer (PTR-ToF 2000, Ionicon, Austria).

207

### 208 **3. RESULTS AND DISCUSSION**

#### 209 **3.1. Characteristics of Sampling Period**

210 A total of five days of CI-API-ToF data were collected successfully, from 2017/06/21 midday  
211 through 2017/06/26 midday. New particle formation events were observed on 24<sup>th</sup> June in the late  
212 afternoon and 25<sup>th</sup> June at midday. Some nighttime formation of molecular clusters was seen  
213 earlier in the campaign, as were several peaks to the 1.5 – 100 nm size range, likely from pollutant  
214 plumes containing freshly nucleating condensable materials. The trace gases, O<sub>3</sub>, SO<sub>2</sub>, NO and NO<sub>2</sub>  
215 are plotted in the Figure S1. O<sub>3</sub> shows mid-afternoon peaks, around ~120 ppb on the first two days  
216 of the campaign, and 50-70 ppb for the latter days. SO<sub>2</sub> shows a large peak, reaching 4 ppb on 22/06  
217 but <1 ppb for the rest of campaign. NO shows strong mid-morning rush hour related peaks,  
218 declining towards midday due to being rapidly consumed by O<sub>3</sub>. NO<sub>2</sub> shows large traffic related  
219 peaks. The sulfuric acid signal across this period as measured by NO<sub>3</sub><sup>-</sup> CI-API-ToF showed strong  
220 midday peaks, with signal highest on 24/06/2017 and 25/06/2017. The meteorological data are  
221 shown in Figure S2 alongside condensation sink (CS). The conditions were generally warm and  
222 humid, with temperature reaching its maximum on 25/06/2017, with a peak hourly temperature of  
223 31°C. High temperatures were seen on 21/06 and 24/06 also, of 30°C and 26°C respectively.

224

#### 225 **3.2. Gas Phase HOM Chemistry**

##### 226 **3.2.1. Bulk chemical properties**

227 For the peaks that have had chemical formulae assigned, oxidation state of carbon, or  $OS_c$ , can be  
228 used to describe their bulk oxidation chemistry.  $OS_c$  is defined as (Kroll et al., 2011)

229

$$OSc = (2 \times O:C) - H:C \quad (2)$$

230  
231  
232  
233  
234  
235  
236  
237  
238  
239  
240  
241  
242  
243  
244  
245  
246  
247  
248  
249  
250  
251

This does not account for the presence of nitrate ester groups, which has been accounted for previously by subtracting five times the N:C ratio (Massoli et al., 2018), under the assumption that all nitrogen containing functionality is in the form of nitrate ester (RONO<sub>2</sub>) groups. In Beijing, multiple sources of nitrate-containing organic compounds are seen, in the forms of amines, nitriles and heterocycles. The variation of oxidation state with carbon number ( $C_n$ ) without correction for nitrate esters is plotted in Figure 1. The average oxidation state of carbon in this dataset tends to decrease with an increase to  $C_n$ , highest where  $C_n = 5$ , attributable both to high O:C and peak area for the peak assigned to C<sub>5</sub>H<sub>10</sub>N<sub>2</sub>O<sub>8</sub> at  $m/Q$  288.  $C_n = 5$  also shows the greatest distribution of oxidation states, likely due to the high ambient concentration of isoprene and therefore its many oxidation products being of high enough signal for many well resolved peaks to be seen in this dataset. It is worth noting that some of the ions plotted here may not form through peroxy radical autoxidation, such as C<sub>5</sub>H<sub>10</sub>N<sub>2</sub>O<sub>8</sub>, which may be a second-generation oxidation product of isoprene under high NO<sub>x</sub> (Lee et al., 2016).  $C_n = 10$  and 15 also see a small increase to average oxidation number compared to their neighbours. The lower oxidation state of the larger products is likely a function of two things. First and foremost, any autoxidation mechanism must undergo more steps in order for a larger molecule to reach an equivalent O:C ratio with a smaller one, and the equivalent O:C ratio is ultimately less likely to be reached before the radical is terminated (Massoli et al., 2018). Secondly, the lower vapour pressures of these larger products will lead to their partitioning into the condensed phase more readily than the smaller, thus they are more rapidly lost (Mutzel et al., 2015).

252  
253  
254  
255

The degrees of OSc observed here are similar to those seen in other environments such as during the SOAS campaign in 2013 in southern United States, characterised by low NO/NO<sub>2</sub> and high temperatures, where campaign averages of 0.3 ppb, 0.4-0.5 ppb, and 25°C respectively were

256 measured, although an additional parameter to account for nitrogen containing VOCs is included in  
257 the calculation (Massoli et al., 2018). The  $OS_c$  observed in Beijing is also higher than that seen in  
258 the boreal forest environment of Hyytiälä, despite extremely low  $NO_x$  concentrations, likely due to  
259 low temperature conditions dominating in those conditions (Schobesberger et al., 2013). These  
260 relatively similar degrees of oxidation to those seen in other, cleaner, environments are likely due to  
261 an interplay between the higher temperatures facilitating rapid hydrogen abstractions (Crouse et  
262 al., 2013; Quéléver et al., 2018) and the higher concentrations of  $NO_x$ ,  $HO_2$ , and other  $RO_2$   
263 molecules terminating the autoxidation sequence more efficiently (Praske et al., 2018, Rissanen,  
264 2018, Garmash et al., 2019).

265  
266 A mass defect plot is shown in Figure 2, which shows nominal mass plotted against mass defect for  
267 all peaks in this dataset. Mass defect is defined as the ion mass minus integer mass. This is shown  
268 for two separate daytime periods, one where nucleation was not occurring and HOM concentrations  
269 are lower (10:30 – 12:00 23/06/2017) and one where nucleation was occurring under high HOM  
270 concentrations (10:30 – 12:00 25/06/2017). The band of lower mass defect is characterised by a  
271 number of large peaks with high signal, for example, at  $m/Q$  436 the ion  $(C_2H_7N)_2(H_2SO_4)_2HSO_4^-$ .  
272 The upper component of the mass defect is dominated by organic compounds, the upper end of  
273 more positive mass defect is occupied by molecules with more  $^1H$  (mass defect 7.825 mDa) and  $^{14}N$   
274 (mass defect 3.074 mDa). The end of less positive mass defect has lower  $^1H$  and more  $^{16}O$  (mass  
275 defect -5.085 mDa); alternatively put, the mass defect reflects the variation in  $OS_c$ . The organic  
276 components with more positive mass defects will be more volatile than their lower mass defect  
277 counterparts as they will contain fewer oxygen functionalities (Tröstl et al., 2016, Stolzenburg et al.,  
278 2018). These higher volatility products may still contribute to larger size particle growth. The more  
279 negative mass defect components will be those of greater O:C and therefore lower volatility,  
280 LVOCs, and the yet larger and more oxidised components, ELVOCs (Tröstl et al., 2016). During  
281 the nucleation period, the signal intensity for the species in the upper band of more negative mass

282 defect have the most marked increase in concentration, with significantly less difference >500 m/Q.  
283 This region 200-400 m/Q will contain most of the C<sub>5</sub>+ monomer HOMs seen in this dataset.

284

### 285 3.2.2. Diurnal trends of HOMs

286 Temporal trends of HOMs in the urban atmosphere can reveal their sources and behaviour in the  
287 atmosphere. Most of the HOM species peak in the daytime. These species all follow a similar  
288 diurnal trend, as shown in Figure 3. Both the concentrations of O<sub>3</sub> and OH· are high during the  
289 summer period in Beijing (although the nitrate chemical ionisation technique is not sensitive to all  
290 OH· oxidation products (Berndt et al., 2015)). Figure S1 shows the time series of concentrations of  
291 NO which is considered a dominant peroxy radical terminator of particular importance in the  
292 polluted urban environment (Khan et al., 2015). Radicals such as HO<sub>2</sub>· and RO<sub>2</sub>· also typically peak  
293 during daytime. The HOM components peaking in the daytime are presumed to be the oxidation  
294 products of a mixture of anthropogenic and biogenic components, such as alkylbenzenes,  
295 monoterpenes and isoprene. The oxidation of monoterpenes, specifically the monoterpene  $\alpha$ -pinene,  
296 has been the subject of extensive study recently, with the O<sub>3</sub>-initiated autoxidation sequence being  
297 the best characterised (Ehn et al., 2014; Jokinen et al., 2014; Kurtén et al., 2015; Kirkby et al.,  
298 2016); ozonolysis of  $\alpha$ -pinene opens the ring structure and produces a RO<sub>2</sub>· radical (Kirkby et al.,  
299 2016). In the case of aromatics, OH· addition to the ring and the subsequently formed bicyclic  
300 peroxy radical is the basis for the autooxidation of compounds such as xylenes and  
301 trimethylbenzenes (Molteni et al., 2018; Wu et al., 2017).

302

303 The identified compounds have been roughly separated into several categories, each of these plotted  
304 in Figure 3. Figure 3 shows the separation of components into non-nitrogen containing HOMs, and  
305 nitrogen containing HOMs, or organonitrates (ONs). The ON signal is much higher than that of the  
306 HOM, attributable in part to a few ions of high signal, such as the isoprene organonitrate  
307 C<sub>5</sub>H<sub>10</sub>N<sub>2</sub>O<sub>8</sub>. A few similar structural formulae are seen (C<sub>5</sub>H<sub>10</sub>N<sub>2</sub>O<sub>6</sub>, C<sub>5</sub>H<sub>11</sub>NO<sub>6</sub>, C<sub>5</sub>H<sub>11</sub>NO<sub>7</sub>, etc),

308 some of which have been identified as important gas phase oxidation products of isoprene under  
309 high  $\text{NO}_x$  conditions (Xiong et al., 2015), and their contribution to SOA has been explored  
310 previously (Lee et al., 2016). A high nitrophenol signal is also seen,  $\text{C}_6\text{H}_5\text{NO}_3$ . The signal for HOM  
311 compounds is less dominated by a few large ions. The prevalence of ON compounds points towards  
312 the important role of  $\text{NO}_x$  as a peroxy radical terminator, with the probability for the  $\text{RO}_2 + \text{NO}_x$   
313 reaction to produce nitrate ester compounds increasing with the size of the  $\text{RO}_2$  molecule (Atkinson  
314 et al., 1982). The  $\text{NO}_x$  concentrations in urban Beijing are approximately a factor of 10 higher than  
315 seen at the Hyytiälä station in Finland as reported by Yan et al. (2016), and hence it is expected to  
316 be a more significant peroxy radical terminator.

317

318 Despite the very large fluxes of anthropogenic organic pollutants in Beijing, biogenic emissions are  
319 still an important source of reactive VOCs in the city, with abundant isoprene oxidation products  
320 observed (see above), as well as monoterpene monomers ( $\text{C}_{10}\text{H}_{16}\text{O}_9$ ,  $\text{C}_{10}\text{H}_{15}\text{O}_9\text{N}$ ) and some dimer  
321 products ( $\text{C}_{20}\text{H}_{30}\text{O}_{11}$ ,  $\text{C}_{20}\text{H}_{31}\text{O}_{11}\text{N}$ ). The time series of the signals of all  $\text{C}_5$ ,  $\text{C}_{10}$  and  $\text{C}_{20}$  molecules is  
322 plotted in Figure 3b, with  $\text{C}_5$  species assumed to be isoprene dominated,  $\text{C}_{10}$  and  $\text{C}_{20}$  assumed to be  
323 monoterpene dominated. Signals for isoprene oxidation products are higher, with abundant  
324 isoprene nitrate and dinitrate products.  $\text{C}_{10}$  products show similar behaviour, with, for example,  
325 several  $\text{C}_{10}\text{H}_{15}\text{O}_x\text{N}$   $x = 5-9$  compounds seen. The  $\text{C}_{20}$  signal intensities are low, and follow the  
326 general formula  $\text{C}_{20}\text{H}_x\text{O}_y\text{N}_z$ , where  $x = 26-32$ ,  $y = 7-11$  and  $z = 0-2$ ; in Figure 3 the signal for  $\text{C}_{20}$   
327 compounds has been multiplied by a factor of 50 for visibility. The low signals reflect the lack of  
328  $\text{RO}_2$  cross reactions necessary for the production of these accretion products.

329

330 Other identified peaks are plotted in Figure 3c. The  $\text{C}_2$ - $\text{C}_4$  components are summed together, these  
331 being small organic acids such as malonic acid and oxalic acid, as well as products such as  
332  $\text{C}_4\text{H}_7\text{O}_6\text{N}$ . Malonic acid is the most prominent here, seen both as an  $\text{NO}_3^-$  adduct ( $\text{C}_3\text{H}_4\text{O}_4\text{NO}_3^-$ ) and  
333 a proton transfer product ( $\text{C}_3\text{H}_3\text{O}_4^-$ ) at a ratio of around 2:3. The  $\text{C}_6$ - $\text{C}_9$  components are assumed to

334 be dominated by oxidation products of alkylbenzenes such as  $C_8H_{12}O_5$ , although fragments of other  
335 compounds, i.e., monoterpenes, can also occupy this region (Isaacman-Vanwertz et al., 2018). It is  
336 assumed the majority of the signal for these peaks come from alkylbenzenes. This assumption is  
337 supported by the relative signal intensity ratios of the oxygen numbers of monomer  $C_8H_{12}O_n$   
338 compounds being similar to those seen for xylene oxidation products in previous work (Molteni et  
339 al., 2018). The largest fraction,  $C_{11}$  through  $C_{18}$ , includes the larger compounds, oxidation products  
340 of larger aromatics, or products of the cross reaction of smaller  $RO_2$  radicals. Here they are grouped  
341 without more sophisticated disaggregation as they all follow much the same time series, species  
342 such as  $C_{11}H_{11}O_8N$  following the same temporal trends as  $C_{15}H_{16}O_9$  and  $C_{16}H_{24}O_{12}$ .

343

344 Nearly all ions with the exception of the larger compounds attributed to the cross reaction of  $C_{10}$   
345 monomers follow similar temporal patterns, with the majority of peaks occurring in the daytime.  
346 This reflects the importance of the concentration of atmospheric oxidants. Some selected oxidation  
347 products are plotted against their precursor VOCs in Figure 4. The concentration of isoprene is  
348 plotted against the signal of a nitrate HOM product,  $C_5H_9NO_6$  (Xiong et al., 2015; Lee et al., 2016),  
349 while monoterpenes are plotted against  $C_{10}H_{16}O_9$  (Ehn et al., 2014; Berndt et al., 2016; Yan et al.,  
350 2016; Kirkby et al., 2016; Massoli et al., 2018), and  $C_2$ -benzenes against  $C_8H_{12}O_6$  (Molteni et al.,  
351 2018; Wang et al., 2017). The first half of the time series shows little correlation between the VOC  
352 species and the resultant oxidation products, while isoprene, monoterpenes and  $C_2$ -benzenes follow  
353 their usual diurnal cycles, isoprene having the most distinct with a strong midday peak. The latter  
354 two days, however, show similar and coinciding peaks in both the VOCs and HOMs - HOMs show  
355 afternoon peaks on both days, and an initial shelf on the final half day. The  $C_5H_9NO_6$  peak follows  
356 some of the peaks of the isoprene, but not all (e.g., morning shelf of isoprene on 24/06).

357 Concentrations of isoprene do not seem to determine directly the signal of HOM, as the day with  
358 the lowest isoprene of all is the day with highest  $C_5H_9NO_6$ . The  $C_{10}H_{16}O_9$  trace has coincidental  
359 peaks with the monoterpene trace also, including two 4-hour separated simultaneous peaks on

360 25/06. The peaks in the concentrations of C<sub>2</sub>-benzenes are nearly synchronous with the peaks in  
361 C<sub>8</sub>H<sub>12</sub>O<sub>6</sub>, for which the data exhibit a strong mid afternoon peak likely due to the lack of an efficient  
362 ozonolysis reaction pathway; the main oxidant of C<sub>2</sub>-benzenes is the OH radical. Trends of both C<sub>3</sub>  
363 benzenes and their HOMs are much the same as C<sub>2</sub> benzenes as discussed above, pointing to similar  
364 sources and oxidation chemistries. . The concentration of precursor VOC is likely a driving force in  
365 the identity and quantity of various HOM products, but not the sole determinant, as while there are  
366 simultaneous peaks of VOCs and HOMs, both the condensation sink and oxidant concentrations  
367 also influence HOM product signals.

368

369 The first half of campaign measurements is marked by an episode of low HOM signals. A diurnal  
370 cycle still exists but it is weak. The radiation intensity was significantly lower on these prior days  
371 than it was on the 24th. No data is available for the final period of measurement. Ozone is higher on  
372 the prior measurement days with lower HOM signals (see Figure S1). It is therefore plausible that  
373 light intensity, and therefore OH concentration is one of the main drivers of HOM concentrations in  
374 Beijing.

375

376 The C<sub>20</sub> compounds plotted in Figure 3b show no strong diurnal sequence, contrasting with other  
377 HOMs. We can presume that all C<sub>20</sub> compounds identified are the result of the reaction of two  
378 monoterpene C<sub>10</sub> RO<sub>2</sub> radicals, a reasonable assumption as all identified C<sub>20</sub> species follow the  
379 general formula outlined for these reactions (C<sub>20</sub>H<sub>28-32</sub>O<sub>6-16</sub>). The formation of C<sub>20</sub> dimers is  
380 dependent upon two processes, initial oxidation of monoterpenes, and RO<sub>2</sub>-RO<sub>2</sub> termination. Initial  
381 oxidation is contingent upon oxidant concentration, which is highest in the daytime, and RO<sub>2</sub>-RO<sub>2</sub>  
382 termination is contingent upon the probability of the molecular collision between the RO<sub>2</sub>  
383 molecules occurring before other radical termination (i.e., RO<sub>2</sub>-NO<sub>x</sub>, or RO<sub>2</sub>-HO<sub>2</sub>). There is likely  
384 a strong diurnal sequence in the dominant RO<sub>2</sub> termination mechanisms across the day period, and  
385 the combination of the two factors discussed above results in there being no strong diurnal trend in

386 these molecules. A lower oxidant concentration at night results in less RO<sub>2</sub> molecules, but less NO  
387 and HO<sub>2</sub> results in a greater chance for those RO<sub>2</sub> molecules to dimerise (Rissanen, 2018, Garmash  
388 et al., 2019). As the levels of NO<sub>x</sub> in Beijing fall, the peroxy radical termination reactions will be  
389 less probable compared to continued autoxidation (Praske et al., 2018), and it is expected that more  
390 oxidised HOM products will be seen with lower volatilities and therefore a greater potential  
391 contribution to earlier stage particle formation and growth.

392

### 393 **3.3. New Particle Formation**

394 Nearly all the signal intensity in the CI-API-ToF instrument arises from molecules charged by NO<sub>3</sub><sup>-</sup>,  
395 therefore plotting the unit mass resolution data (the data gained by integrating over the entire area at  
396 each m/Q integer) against time describes simply the evolution of oxidised organic molecules, acids  
397 and their molecular clusters both with each other and stabilising amine species. This is done in  
398 Figure 5. As the signal intensity varies by factors of 10 from mass to mass, each value has been  
399 normalised so they have maxima at 1. This has been done separately for two days for clarity, as the  
400 signal intensity also varies from day to day. PSM data for these two days is plotted in Figure 5 also,  
401 with both total particle count >1.30 nm in black and the number difference between the lower and  
402 upper size cuts (1.30 and 1.84 nm) in blue, which shows the number of particles between these  
403 sizes. The relationship between mass and electrical mobility diameter can be defined thus (Tammet,  
404 1995),

$$405 \quad d_e = \left(\frac{6m}{\pi\rho}\right)^{\frac{1}{3}} + d_g \quad (3)$$

406

407 where  $d_e$  is the electrical mobility diameter of the cluster or particle,  $m$  is the mass of the cluster or  
408 particle expressed in kg,  $\rho$  is the density and  $d_g$  is the effective gas diameter, determined to be 0.3  
409 nm for smaller particles (Larriba et al., 2011). We can use this to draw a comparison between the  
410 PSM and CI-API-ToF measurements. If a density of 1.2 g cm<sup>-3</sup> is assumed, then once molecular  
411 clusters reach the >400  $m/Q$  range, they will be seen in the lowest size cut of the PSM, or >700  $m/Q$



412 if a density of  $2.0 \text{ g cm}^{-3}$  is assumed. A full table of densities is provided in the Supplementary  
413 Information.

414

415 A burst in the signal seen by the CI-APi-TOF occurs first in the late morning in the top panel of  
416 Figure 5, and this is at the same time as peaks begin to rise in the identified HOMs (see Figure 3).  
417 Here, the PSM is not available due to an instrumental fault until 16:00; however, at that point, an  
418 elevation to particle count and a large elevation to cluster count can be seen. Moving into the  
419 evening period, the mass contour shows peaks to larger masses  $>400 \text{ m/Q}$ . This is likely dimerised  
420 compounds and products of  $\text{NO}_3^-$  chemistry with little contribution to newly forming particles, but  
421 still sensitive to chemical ionisation by  $\text{NO}_3^-$ . Many of these peaks cannot be assigned due to  
422 uncertainties in the structural formula assignment for higher mass peaks, as the number of possible  
423 dimerised compounds is many, being the combination of most possible  $\text{RO}_2$  radicals. Graphically,  
424 these are over-represented in Figure 5 due to the normalisation, their signals (especially  $>500 \text{ m/Q}$ )  
425 are much lower than the signals  $<400 \text{ m/Q}$ .

426

427 The second day plotted in the lower panel of Figure 5 (25/06/2017) shows a strong afternoon peak  
428 to the HOMs (for most HOMs, stronger than that on the day prior). Particle formation is shown in  
429 the PSM data. A strong midday peak to particle number is seen with two distinct peaks to cluster  
430 count. These two peaks are not coincidental with the two peaks to HOM signal (i.e., nitrogen-  
431 containing HOMs in Figure 3a peaking at 11:00 and 16:00). Sulfuric acid, however, does peak  
432 synchronously with the particle number count. Sulfuric acid is plotted across the contour plot in  
433 Figure 6, where PSM data is also shown in the bottom panel. The peak to CI-APi-TOF mass signal,  
434 visible in Figure 5 occurs at around 12:00/13:00, peaks in the PSM cluster count occur at 10:00 and  
435 13:00. Peaks in mass up to  $550 \text{ m/Q}$  are seen in the CI-APi-ToF at 13:00. Assuming the density of  
436 these species is  $\leq 1.6 \text{ g cm}^{-3}$  then these will be suitably sized to be grown in the PSM saturator..  
437 These newly formed particles then go on to grow and contribute significantly to the larger particle

438 count (Figure S3). As initial particle formation coincides with sulfuric acid signal peaks and before  
439 HOM signals peak, it can be assumed on these days, the HOM contribution to the initial particle  
440 formation is modest.

441

442 There is recent strong evidence to suggest that the driving force of the earliest stages of particle  
443 formation in urban Shanghai is from sulfuric acid and C<sub>2</sub>-amines (Yao et al., 2018), and the  
444 coincidental peaks of sulfuric acid with new particles as seen in Figure 6 suggest a similar  
445 behaviour. Dimethylamine (DMA) can efficiently stabilise the sulfuric acid clusters (Almeida et al.,  
446 2013). Here, few larger sulfuric acid-DMA clusters were visible in the dataset, as seen in the work  
447 by Yao et al., 2018, although five sulfuric acid-dimethylamine (SA-DMA) ions were observed, the  
448 others were likely too low in signal to be confidently resolved from their neighbouring peaks;  
449 however, clusters of up to 4 sulfuric acid ions and 3 dimethylamine molecules were seen, with  
450 similar diurnal trends to sulfuric acid. The scarcity of SA-DMA clusters is likely due to  
451 instrumental conditions, rather than their absence in the atmosphere. The nitrate chemical ionisation  
452 system tends to evaporate amine compounds upon charging, and as specific voltage-tuning setups  
453 can lend themselves towards preservation or breakage of molecular clusters, the signal for larger  
454 sulfuric acid clusters was also very weak. The formation of HOM-sulfuric acid clusters is unlikely  
455 under atmospheric conditions (Elm et al., 2017) and few of these were observed. Signals of HOMs  
456 seem to coincide with later particle growth; it can be expected that HOM molecules make a more  
457 significant contribution to particle growth than to early particle formation, with the largest and most  
458 oxidised being involved in early growth, and the smaller and less oxidised contributing to later  
459 growth as the necessary vapour pressure properties become less demanding.

460

#### 461 **4. CONCLUSIONS**

462 The average degree of HOM oxidation in Beijing is comparable with that seen in other  
463 environments. Rapid intramolecular hydrogen shifts during autoxidation due to the higher

464 temperatures are probably offset by the frequent termination reactions due to high  $\text{NO}_x$   
465 concentrations.  $OS_c$  values seem to be marginally higher for biogenic species.  
466

467 The temporal trend of nearly every HOM shows afternoon or evening maxima. Both  $\text{O}_3$  and OH  
468 have high daytime concentrations and these likely drive the initial oxidation steps. The species  
469 arising from alkylbenzene precursors show sharper afternoon peaks, probably since their oxidation  
470 is OH dominated. Many of the rest of the peaks, coming from largely BVOC precursors show  
471 broader daytime peaks, being influenced by  $\text{O}_3$  also. There seems to be no direct link between VOC  
472 concentrations and HOM signals, with days of lower precursor VOC sometimes having higher  
473 HOM signals and vice versa.

474

475 Initial particle formation coincides with peak sulfuric acid signals, while the growth of the particles  
476 correlates more closely with the signals of HOMs. This is very similar to behaviour observed in a  
477 study of NPF in Shanghai which was attributed to sulfuric acid-dimethylamine-water nucleation  
478 with condensing organic species contributing to particle growth (Yao et al., 2018), and this is  
479 further backed up by numerous SA-DMA clusters present in this dataset. The freshly formed  
480 particles grow and contribute significantly to total particle loading. This is visible when the unit  
481 mass CI-APi-ToF data is plotted as a contour plot, and further to this is visible in the PSM data,  
482 with bursts to both total number count  $>1.30$  nm and the number of molecular clusters between 1.30  
483 and 1.84 nm. As  $\text{NO}_x$  levels fall in Beijing due to traffic emission control measures being enforced  
484 it is likely that autoxidation will become increasingly significant in the new particle formation  
485 processes. The number of molecules detected by the  $\text{NO}_3$  CIMS is undoubtedly many more than  
486 have had formulae assigned here, but to identify more requires a more sophisticated data  
487 deconvolution.

488

489

490 **DATA ACCESSIBILITY**

491 Data supporting this publication are openly available from the UBIRA eData repository at  
492 <https://doi.org/10.25500/edata.bham.00000304>

493

494 **AUTHOR CONTRIBUTIONS**

495 The study was conceived and planned by RMH and ZS. DCSB and JB set up and operated the  
496 main instrumental measurements, and JB prepared the first draft of the paper and responded to  
497 comments from RMH and ZS. CNH and WJA contributed the hydrocarbon data and provided  
498 comments on the draft manuscript, and ES and JL contributed the gas phase pollutant data.

499

500 **COMPETING INTERESTS**

501 The authors have no conflict of interests.

502

503 **ACKNOWLEDGMENTS**

504 This work was part of the APHH-Beijing programme funded by the UK Natural Environment  
505 Research Council (NE/N007190/1) and the Natural Sciences Funding Council of China. It was  
506 additionally facilitated by the National Centre for Atmospheric Science ODA national capability  
507 programme ACREW (NE/R000034/1), which is supported by NERC and the GCRF. We thank  
508 Professor X.M Wang from the Guangzhou Institute of Geochemistry, Chinese Academy of  
509 Sciences, Brian Davison from Lancaster University and Ben Langford, Eiko Nemitz, Neil  
510 Mullinger and other staff from the Centre for Ecology and Hydrology, Edinburgh for assistance  
511 with the VOC measurements and associated infrastructure.

512

513 **REFERENCES**

514

515 Alam, A., Shi, J.P., Harrison R.M.: Observations of new particle formation in urban air, *J. Geophys.*  
516 *Res.*, 108, 4093-4107, doi:10.1029/2001JD001417, 2003

517

518 Almeida, J., Schobesberger, S., Kürten, A., Ortega, I. K., Kupiainen-Määttä, O., Praplan, A. P.,  
519 Adamov, A., Amorim, A., Bianchi, F., Breitenlechner, M., David, A., Dommen, J., Donahue, N.  
520 M., Downard, A., Dunne, E., Duplissy, J., Ehrhart, S., Flagan, R. C., Franchin, A., Guida, R.,  
521 Hakala, J., Hansel, A., Heinritzi, M., Henschel, H., Jokinen, T., Junninen, H., Kajos, M.,  
522 Kangasluoma, J., Keskinen, H., Kupc, A., Kurtén, T., Kvashin, A. N., Laaksonen, A., Lehtipalo, K.,  
523 Leiminger, M., Leppä, J., Loukonen, V., Makhmutov, V., Mathot, S., McGrath, M. J., Nieminen,  
524 T., Olenius, T., Onnela, A., Petäjä, T., Riccobono, F., Riipinen, I., Rissanen, M., Rondo, L.,  
525 Ruuskanen, T., Santos, F. D., Sarnela, N., Schallhart, S., Schnitzhofer, R., Seinfeld, J. H., Simon,  
526 M., Sipilä, M., Stozhkov, Y., Stratmann, F., Tomé, A., Tröstl, J., Tsagkogeorgas, G., Vaattovaara,  
527 P., Viisanen, Y., Virtanen, A., Vrtala, A., Wagner, P. E., Weingartner, E., Wex, H., Williamson, C.,  
528 Wimmer, D., Ye, P., Yli-Juuti, T., Carslaw, K. S., Kulmala, M., Curtius, J., Baltensperger, U.,  
529 Worsnop, D. R., Vehkamäki, H., and Kirkby, J.: Molecular understanding of sulphuric acid-amine  
530 particle nucleation in the atmosphere, *Nature*, 502, 359-363, 2013.

531

532 Atkinson, R., Aschmann, S. M., Carter, W. P. L., Winer, A. M., and Pitts, J. N.: Alkyl nitrate  
533 formation from the nitrogen oxide (NO<sub>x</sub>)air photooxidations of C<sub>2</sub>-C<sub>8</sub> n-alkanes, *J. Phys. Chem.*,  
534 86, 4563-4569, 1982.

535

536 Berndt, T., Richters, S., Kaethner, R., Voigtländer, J., Stratmann, F., Sipilä, M., Kulmala, M., and  
537 Herrmann, H.: Gas-Phase Ozonolysis of Cycloalkenes: Formation of Highly Oxidized RO<sub>2</sub>  
538 Radicals and Their Reactions with NO, NO<sub>2</sub>, SO<sub>2</sub>, and Other RO<sub>2</sub> Radicals, *J. Phys. Chem. A.*,  
539 119, 10336-10348, 2015.

540

541 Berndt, T., Richters, S., Jokinen, T., Hyttinen, N., Kurtén, T., Otkjær, R. V., Kjaergaard, H. G.,  
542 Stratmann, F., Herrmann, H., Sipilä, M., Kulmala, M., and Ehn, M.: Hydroxyl radical-induced  
543 formation of highly oxidized organic compounds, *Nature Comm.*, 7, 20  
544 <https://doi.org/10.1038/ncomms13677>, 2016.

545

546 Bianchi, F., Garmash, O., He, X., Yan, C., Iyer, S., Rosendahl, I., Xu, Z., Rissanen, M. P., Riva, M.,  
547 Taipale, R., Sarnela, N., Petäjä, T., Worsnop, D. R., Kulmala, M., Ehn, M., and Junninen, H.: The  
548 role of highly oxygenated molecules (HOMs) in determining the composition of ambient ions in the  
549 boreal forest, *Atmos. Chem. Phys.*, 17, 13819-13831, 2017.

550

551 Brook, R. D., Rajagopalan, S., Pope, C. A., Brook, J. R., Bhatnagar, A., Diez-Roux, A. V., Holguin,  
552 F., Hong, Y., Luepker, R. V., Mittleman, M. A., Peters, A., Siscovick, D., Smith, S. C., Whitsel, L.,  
553 and Kaufman, J. D.: Particulate matter air pollution and cardiovascular disease: An update to the  
554 scientific statement from the american heart association, *Circulation*, 121, 2331-2378, 2010.

555

556 Chu, B., Kerminen, V.-M., Bianchi, F., Yan, C., Petaja, T., and Kulmala, M.: Atmospheric new  
557 particle formation in China, *Atmos. Chem. Phys.*, 19, 115-138, 2019.

558

559 Crouse, J. D., Nielsen, L. B., Jørgensen, S., Kjaergaard, H. G., and Wennberg, P. O.: Autoxidation  
560 of organic compounds in the atmosphere, *J. Phys. Chem. Lett.*, 4, 3513-3520, 2013.

561

562

563

564 Cubison, M. J. and Jimenez, J. L.: Statistical precision of the intensities retrieved from constrained  
565 fitting of overlapping peaks in high resolution mass spectra, *Atmos. Meas. Tech.*, 8, 2333-2345,  
566 2015.

567

568 Delfino, R. J., Sioutas, C., and Malik, S.: Potential role of ultrafine particles in associations between  
569 airborne particle mass and cardiovascular health, *Environ. Health Perspect.*, 113, 934-946, 2005.

570

571 Ehn, M., Thornton, J. A., Kleist, E., Sipilä, M., Junninen, H., Pullinen, I., Springer, M., Rubach, F.,  
572 Tillmann, R., Lee, B., Lopez-Hilfiker, F., Andres, S., Acir, I.-H., Rissanen, M., Jokinen, T.,  
573 Schobesberger, S., Kangasluoma, J., Kontkanen, J., Nieminen, T., Kurtén, T., Nielsen,  
574 L. B., Jørgensen, S., Kjaergaard, H. G., Canagaratna, M., Maso, M. D., Berndt, T., Petäjä, T.,  
575 Wahner, A., Kerminen, V.-M., Kulmala, M., Worsnop, D. R., Wildt, J., and Mentel, T. F.: A large  
576 source of low-volatility secondary organic aerosol, *Nature*, 506, 476-479, 2014.

577

578 Elm, J., Myllys, N., and Kurtén, T.: What is Required for Highly Oxidized Molecules to Form  
579 Clusters with Sulfuric Acid?, *J. Phys. Chem. A*, 121, 4578-4587, 2017.

580

581 Garmash, O., Rissanen, M. P., Pullinen, I., Schmitt, S., Kausiala, O., Tillmann, R., Percival, C.,  
582 Bannan, T. J., Priestley, M., Hallquist, Å. M., Kleist, E., Kiendler-Scharr, A., Hallquist, M., Berndt,  
583 T., McFiggans, G., Wildt, J., Mentel, T., and Ehn, M.: Multi-generation OH oxidation as a source  
584 for highly oxygenated organic molecules from aromatics, *Atmos. Chem. Phys. Discuss.*,  
585 <https://doi.org/10.5194/acp-2019-582>, in review, 2019.

586

587 Gong, Y., Hu, M., Cheng, Y., Su, H., Yue, D., Liu, F., Wiedensohler, A., Wang, Z., Kalesse, H.,  
588 Liu, S., Wu, Z., Xiao, K., Mi, P., and Zhang, Y.: Competition of coagulation sink and source rate:  
589 New particle formation in the Pearl River Delta of China, *Atmos. Environ.*, 44, 3278-3285, 2010.

590

591 Guo, S., Hu, M., Zamora, M. L., Peng, J., Shang, D., Zheng, J., Du, Z., Wu, Z., Shao, M., Zeng, L.,  
592 Molina, M. J., and Zhang, R.: Elucidating severe urban haze formation in China., *PNAS*, 111,  
593 17373- 17378, 2014.

594

595 Hyttinen, N., Kupiainen-Määttä, O., Rissanen, M. P., Muuronen, M., Ehn, M., and Kurtén, T.:  
596 Modeling the Charging of Highly Oxidized Cyclohexene Ozonolysis Products Using Nitrate-Based  
597 Chemical Ionization, *J. Phys. Chem., A*, 119, 6339-6345, 2015.

598

599 Isaacman-Vanwertz, G., Massoli, P., O'Brien, R., Lim, C., Franklin, J. P., Moss, J. A., Hunter, J. F.,  
600 Nowak, J. B., Canagaratna, M. R., Misztal, P. K., Arata, C., Roscioli, J. R., Herndon, S. T., Onasch,  
601 T. B., Lambe, A. T., Jayne, J. T., Su, L., Knopf, D. A., Goldstein, A. H., Worsnop, D. R., and Kroll,  
602 J. H.: Chemical evolution of atmospheric organic carbon over multiple generations of oxidation,  
603 *Nature Chem.*, 10, 462-468, <https://doi.org/10.1038/s41557-018-0002-2>, 2018

604

605 Jokinen, T., Sipilä, M., Junninen, H., Ehn, M., Lönn, G., Hakala, J., Petäjä, T., Mauldin, R. L.,  
606 Kulmala, M., and Worsnop, D. R.: Atmospheric sulphuric acid and neutral cluster measurements  
607 using CI-APi-TOF, *Atmos. Chem. Phys.*, 12, 4117-4125, 2012.

608

609 Jokinen, T., Sipilä, M., Richters, S., Kerminen, V. M., Paasonen, P., Stratmann, F., Worsnop, D.,  
610 Kulmala, M., Ehn, M., Herrmann, H., and Berndt, T.: Rapid autoxidation forms highly oxidized  
611 RO<sub>2</sub> radicals in the atmosphere, *Angewandte Chemie - International Edition*, 53, 14596-14600,  
612 <https://doi.org/10.1002/anie.201408566>, 2014.

613

614

615 Junninen, H., Ehn, M., Petäjä, Luosujärvi, L., Kotiaho, T., Kostianen, R., Rohner, U., Gonin, M.,  
616 Fuhrer, K., Kulmala, M., and Worsnop, D. R.: A high-resolution mass spectrometer to measure  
617 atmospheric ion composition, *Atmos. Meas. Tech.*, 3, 1039-1053, 2010.  
618

619 Kerminen, V. M., Paramonov, M., Anttila, T., Riipinen, I., Fountoukis, C., Korhonen, H., Asmi, E.,  
620 Laakso, L., Lihavainen, H., Swietlicki, E., Svenningsson, B., Asmi, A., Pandis, S. N., Kulmala, M.,  
621 and Petäjä, T.: Cloud condensation nuclei production associated with atmospheric nucleation: A  
622 synthesis based on existing literature and new results, *Atmos. Chem. Phys.*, 12, 12037-12059, 2012.  
623

624 Khan, M., Cooke M, Utembe, S., Archibald A., Derwent, R., Jenkin, M., Morris, W., South, N.,  
625 Hansen, J., Francisco, J., Percival, C., Shallcross, D.: Global analysis of peroxy radicals and peroxy  
626 radical-water complexation using the STOCHEM-CRI global chemistry and transport model,  
627 *Atmos. Environ.*, 106, 278-287, 2015.  
628

629 Kirkby, J., Curtius, J., Almeida, J., Dunne, E., Duplissy, J., Ehrhart, S., Franchin, A., Gagné, S.,  
630 Ickes, L., Kürten, A., Kupc, A., Metzger, A., Riccobono, F., Rondo, L., Schobesberger, S.,  
631 Tsagkogeorgas, G., Wimmer, D., Amorim, A., Bianchi, F., Breitenlechner, M., David, A.,  
632 Dommen, J., Downard, A., Ehn, M., Flagan, R. C., Haider, S., Hansel, A., Hauser, D., Jud, W.,  
633 Junninen, H., Kreissl, F., Kvashin, A., Laaksonen, A., Lehtipalo, K., Lima, J., Lovejoy, E. R.,  
634 Makhmutov, V., Mathot, S., Mikkilä, J., Minginette, P., Mogo, S., Nieminen, T., Onnela, A.,  
635 Pereira, P., Petäjä, T., Schnitzhofer, R., Seinfeld, J. H., Sipilä, M., Stozhkov, Y., Stratmann, F.,  
636 Tomé, A., Vanhanen, J., Viisanen, Y., Vrtala, A., Wagner, P. E., Walther, H., Weingartner, E.,  
637 Wex, H., Winkler, P. M., Carslaw, K. S., Worsnop, D. R., Baltensperger, U., and Kulmala, M.:  
638 Role of sulphuric acid, ammonia and galactic cosmic rays in atmospheric aerosol nucleation,  
639 *Nature*, 476, 429-435, <https://doi.org/10.1038/nature10343>, 2011.  
640

641 Kirkby, J., Duplissy, J., Sengupta, K., Frege, C., Gordon, H., Williamson, C., Heinritzi, M., Simon,  
642 M., Yan, C., Almeida, J., Trostl, J., Nieminen, T., Ortega, I. K., Wagner, R., Adamov, A., Amorim,  
643 A., Bernhammer, A. K., Bianchi, F., Breitenlechner, M., Brilke, S., Chen, X., Craven, J., Dias, A.,  
644 Ehrhart, S., Flagan, R. C., Franchin, A., Fuchs, C., Guida, R., Hakala, J., Hoyle, C. R., Jokinen, T.,  
645 Junninen, H., Kangasluoma, J., Kim, J., Krapf, M., Kurten, A., Laaksonen, A., Lehtipalo, K.,  
646 Makhmutov, V., Mathot, S., Molteni, U., Onnela, A., Perakyla, O., Piel, F., Petaja, T., Praplan, A.  
647 P., Pringle, K., Rap, A., Richards, N. A., Riipinen, I., Rissanen, M. P., Rondo, L., Sarnela, N.,  
648 Schobesberger, S., Scott, C. E., Seinfeld, J. H., Sipilä, M., Steiner, G., Stozhkov, Y., Stratmann, F.,  
649 Tomé, A., Virtanen, A., Vogel, A. L., Wagner, A. C., Wagner, P. E., Weingartner, E., Wimmer, D.,  
650 Winkler, P. M., Ye, P., Zhang, X., Hansel, A., Dommen, J., Donahue, N. M., Worsnop, D. R.,  
651 Baltensperger, U., Kulmala, M., Carslaw, K. S., and Curtius, J.: Ion-induced nucleation of pure  
652 biogenic particles, *Nature*, 533, 521-526, <https://doi.org/10.1038/nature17953>, 2016.  
653

654 Kroll, J. H., Donahue, N. M., Jimenez, J. L., Kessler, S. H., Canagaratna, M. R., Wilson, K. R.,  
655 Altieri, K. E., Mazzoleni, L. R., Wozniak, A. S., Bluhm, H., Mysak, E. R., Smith, J. D., Kolb, C. E.,  
656 and Worsnop, D. R.: Carbon oxidation state as a metric for describing the chemistry of atmospheric  
657 organic aerosol, *Nature Chemistry*, 3, 133-139, <https://doi.org/10.1038/nchem.948>, 2011.  
658

659 Kulmala, M., Petäjä, T., Mönkkönen, P., Koponen, I. K., Dal Maso, M., Aalto, P. P., Lehtinen, K.  
660 E. J., and Kerminen, V.-M.: On the growth of nucleation mode particles: source rates of  
661 condensable vapor in polluted and clean environments, *Atmos. Chem. Phys.*, 5, 409-416, 2005.  
662

663 Kulmala, M., Petäjä, T., Nieminen, T., Sipilä, M., Manninen, H. E., Lehtipalo, K., Dal Maso, M.,  
664 Aalto, P. P., Junninen, H., Paasonen, P., Riipinen, I., Lehtinen, K. E. J., Laaksonen, A., and  
665 Kerminen, V.-M.: Measurement of the nucleation of atmospheric aerosol particles, *Nature*  
666 *Protocols*, 7, 1651-1667, <https://doi.org/10.1038/nprot.2012.091>, 2012.

667 Kürten, A., Rondo, L., Ehrhart, S., and Curtius, J.: Calibration of a chemical ionization mass  
668 spectrometer for the measurement of gaseous sulfuric acid, *J. Phys. Chem., A*, 116, 6375-6386.  
669

670 Kurtén, T., Rissanen, M. P., Mackeprang, K., Thornton, J. A., Hyttinen, N., Jørgensen, S., Ehn, M.,  
671 and Kjaergaard, H. G.: Computational Study of Hydrogen Shifts and Ring-Opening Mechanisms in  
672  $\alpha$ -Pinene Ozonolysis Products, *J. Phys. Chem., A*, 119, 11366-11375, 2015.  
673

674 Kurtén, T., Tiusanen, K., Roldin, P., Rissanen, M., Luy, J. N., Boy, M., Ehn, M., and Donahue, N.:  
675  $\alpha$ -Pinene autoxidation products may not have extremely low saturation vapor pressures despite high  
676 O:C ratios, *J. Phys. Chem., A*, 120, 2569-2582, 2016.  
677

678 Larriba, C., Hogan, C. J., Attoui, M., Borrajo, R., Garcia, J. F., and De La Mora, J. F.: The  
679 mobility-volume relationship below 3.0 nm examined by tandem mobility-mass measurement,  
680 *Aerosol Sci. Techn.*, 45, 453-467, 2011.  
681

682 Lee, B. H., Mohr, C., Lopez-Hilfiker, F. D., Lutz, A., Hallquist, M., Lee, L., Romer, P., Cohen, R.  
683 C., Iyer, S., Kurtén, T., Hu, W., Day, D. A., Campuzano-Jost, P., Jimenez, J. L., Xu, L., Ng, N. L.,  
684 Guo, H., Weber, R. J., Wild, R. J., Brown, S. S., Koss, A., de Gouw, J., Olson, K., Goldstein, A. H.,  
685 Seco, R., Kim, S., McAvey, K., Shepson, P. B., Starn, T., Baumann, K., Edgerton, E. S., Liu, J.,  
686 Shilling, J. E., Miller, D. O., Brune, W., Schobesberger, S., D'Ambro, E. L., and Thornton, J. A.:  
687 Highly functionalized organic nitrates in the southeast United States: Contribution to secondary  
688 organic aerosol and reactive nitrogen budgets, *PNAS*, 113, 1516-1521, 2016.  
689

690 Lehtipalo, K., Yan, C., Dada, L., Bianchi, F., Xiao, M., Wagner, R., Stolzenburg, D., Ahonen, L. R.,  
691 Amorim, A., Baccarini, A., Bauer, P. S., Baumgartner, B., Bergen, A., Bernhammer, A.,  
692 K., Breitenlechner, M., Brilke, S., Buchholz, A., Mazon, S. B., Chen, D., Chen, X., Dias, A.,  
693 Dommen, J., Draper, D. C., Duplissy, J., Ehn, M., Finkenzeller, H., Fischer, L., Frege, C., Fuchs,  
694 C., Garmash, O., Gordon, H., Hakala, J., He, X., Heikkinen, L., Heinritzi, M., Helm, J. C., Hofbauer,  
695 V., Hoyle, C. R., Joki-nen, T., Kangasluoma, J., Kerminen, V.-M., Kim, C., Kirkby, J., Kontkanen,  
696 J., Kürten, A., Lawler, M. J., Mai, H., Mathot, S., Mauldin, R. L., Molteni, U., Nichman, L., Nie,  
697 W., Niemi-nen, T., Ojdanic, A., Onnela, A., Passananti, M., Petäjä, T., Piel, F., Pospisilova, V.,  
698 Quéléver, L. L. J., Rissanen, M. P., Rose, C., Sarnela, N., Schallhart, S., Schuchmann, S., Sengupta,  
699 K., Simon, M., Sipilä, M., Tauber, C., Tomé, A., Tröstl, J., Väisänen, O., Vogel, A. L., Volkamer,  
700 R., Wagner, A. C., Wang, M., Weitz, L., Wimmer, D., Ye, P., Ylisirniö, A., Zha, Q., Carslaw, K. S.,  
701 Curtius, J., Donahue, N. M., Flagan, R. C., Hansel, A., Riipinen, I., Virtanen, A., Winkler, P. M.,  
702 Baltensperger, U., Kulmala, M., and Worsnop, D. R.: Multicomponent new particle formation from  
703 sulfuric acid, ammonia, and biogenic vapors, *Science Advances*, 4,  
704 <https://doi.org/10.1126/sciadv.aau5363>, 2018.  
705

706 Massoli, P., Stark, H., Canagaratna, M. R., Krechmer, J. E., Xu, L., Ng, N. L., Mauldin, R. L., Yan,  
707 C., Kimmel, J., Misztal, P. K., Jimenez, J. L., Jayne, J. T., and Worsnop, D. R.: Ambient  
708 Measurements of Highly Oxidized Gas-Phase Molecules during the Southern Oxidant and Aerosol  
709 Study (SOAS) 2013, *ACS Earth Space Chem.*, 2, 653-672, 2018.  
710

711 McMurry, P. H., Shan Woo, K., Weber, R., Chen, D.-R., and Pui, D. Y. H.: Size distributions of 3-  
712 10 nm atmospheric particles: implications for nucleation mechanisms, *Philosophical Transactions*  
713 *of the Royal Society A: Math., Phys. Eng. Sci.*, 358, 2625-2642, 2000.  
714

715 Miller, M. R., Raftis, J. B., Langrish, J. P., McLean, S. G., Samutrtai, P., Connell, S. P., Wilson, S.,  
716 Vesey, A. T., Fokkens, P. H., Boere, A. J. F., Krystek, P., Campbell, C. J., Hadoke, P. W.,  
717 Donaldson, K., Cassee, F. R., Newby, D. E., Duffin, R., and Mills, N. L.: Inhaled nanoparticles  
718 accumulate at sites of vascular disease, *ACS Nano*, 11, 4542-4552, 2017.



719 Møller, K. H., Tram, C. M., and Kjaergaard, H. G.: Side-by-Side Comparison of Hydroperoxide  
720 and Corresponding Alcohol as HydrogenBond Donors, *J. Phys. Chem. A*, 121, 2951-2959, 2017.  
721

722 Molteni, U., Bianchi, F., Klein, F., Haddad, I. E., Frege, C., Rossi, M. J., Dommen, J., and  
723 Baltensperger, U.: Formation of highly oxygenated organic molecules from aromatic compounds,  
724 *Atmos. Chem. Phys.*, 18, 1909-1921, 2018.  
725

726 Mutzel, A., Poulain, L., Berndt, T., Iinuma, Y., Rodigast, M., Böge, O., Richters, S., Spindler, G.,  
727 Sipila, M., Jokinen, T., Kulmala, M., Herrmann, H.: Highly oxidized multifunctional organic  
728 compounds observed in tropospheric particles: A field and laboratory study, *Environ. Sci. Technol.*,  
729 49, 7754-7761, 2015.  
730

731 Myllys, N., Olenius, T., Kurtén, T., Vehkamäki, H., Riipinen, I., and Elm, J.: Effect of Bisulfate,  
732 Ammonia, and Ammonium on the Clustering of Organic Acids and Sulfuric Acid, *J. Phys. Chem.*  
733 *A*, 121, 4812-4824, 2017.  
734

735 Penner, J. E., Xu, L., and Wang, M.: Satellite methods underestimate indirect climate forcing by  
736 aerosols., *PNAS*, 108, 13404-13408, 2011.  
737

738 Praske, E., Otkjær, R. V., Crounse, J. D., Hethcox, J. C., Stoltz, B. M., Kjaergaard, H. G., and  
739 Wennberg, P. O.: Atmospheric autoxidation is increasingly important in urban and suburban North  
740 America, *PNAS*, 115, 64-69, 2018.  
741

742 Qi, X., Ding, A., Roldin, P., Xu, Z., Zhou, P., Sarnela, N., Nie, W., Huang, X., Rusanen, A., Ehn,  
743 M., Rissanen, M. P., Petäjä, T., Kulmala, M., and Boy, M.: Modelling studies of HOMs and their  
744 contributions to new particle formation and growth: comparison of boreal forest in Finland and a  
745 polluted environment in China, *Atmos. Chem. Phys.*, 18, 11779-11791, 2018.  
746

747 Quéléver, J., Kristensen, K., Normann Jensen, L., Teiwes, R., Daellenbach, Kaspar R., Peräkylä, O.,  
748 Roldin, P., Pedersen, H., Glasius, M., Bilde, M., Ehn, M.: Effect of temperature on the formation of  
749 Highly-oxygenated Organic Molecules (HOM) from alpha-pinene ozonolysis, *Atmos. Chem. Phys.*  
750 *Discuss.*, 18, 1-29, 2018.  
751

752 Riccobono, F., Schobesberger, S., Scott, C., Dommen, J., Ortega, I., Rondo, L., Almeida, J.,  
753 Amorim, A., Bianchi, F., Breitenlechner, M., David, A., Downard, A., Dunne, E., Duplissy, J.,  
754 Ehrhart, S., Flagan, R., Franchin, A., Hansel, A., Junninen, H., Kajos, M., Keskinen, H., Kupc, A.,  
755 Kürten, A., Kvashin, A., Laaksonen, A., Lehtipalo, K., Makhmutov, V., Mathot, S., Nieminen, T.,  
756 Onnela, A., Petäjä, T., Praplan, A., Santos, F., Schallhart, S., Seinfeld, J., Sipilä, M., Van Spracklen,  
757 D., Stozhkov, Y., Stratmann, F., Tomé, A., Tsagkogeorgas, G., Vaattovaara, P., Viisanen, Y.,  
758 Vrtala, A., Wagner, P., Weingartner, E., Wex, H., Wimmer, D., Carslaw, K., Curtius, J., Donahue,  
759 N., Kirkby, J., Kulmala, M., Worsnop, D., and Baltensperger, U.: Oxidation products of biogenic  
760 emissions contribute to nucleation of atmospheric particles, *Science*, 344, 717-721, 2014.  
761

762 Rissanen, M. P., Kurtén, T., Sipilä, M., Thornton, J. A., Kangasluoma, J., Sarnela, N., Junninen, H.,  
763 Jørgensen, S., Schallhart, S., Kajos, M. K., Taipale, R., Springer, M., Mentel, T. F., Ruuskanen, T.,  
764 Petäjä, T., Worsnop, D. R., Kjaergaard, H. G., and Ehn, M.: The formation of highly oxidized  
765 multifunctional products in the ozonolysis of cyclohexene, *J. Am. Chem. Soc.*, 136, 15596-15606  
766 2014.  
767

768 Rissanen, M. P.: NO<sub>2</sub> Suppression of Autoxidation–Inhibition of Gas-Phase Highly Oxidized Dimer  
769 Product Formation, *ACS Earth Space Chem.*, 2, 1211–1219,  
770 <https://doi.org/10.1021/acsearthspacechem.8b00123>, 2018.

771 Rose, C., Zha, Q., Dada, L., Yan, C., Lehtipalo, K., Junninen, H., Mazon, S. B., Jokinen, T.,  
772 Sarnela, N., Sipilä, M., Petäjä, T., Kerminen, V.-M., Bianchi, F., and Kulmala, M.: Observations of  
773 biogenic ion-induced cluster formation in the atmosphere, *Sci. Adv.*, 4, eaar5218,  
774 <https://doi.org/10.1126/sciadv.aar5218>, 2018.

775  
776 Schobesberger, S., Junninen, H., Bianchi, F., Lönn, G., Ehn, M., Lehtipalo, K., Dommen, J.,  
777 Ehrhart, S., Ortega, I. K., Franchin, A., Nieminen, T., Riccobono, F., Hutterli, M., Duplissy, J.,  
778 Almeida, J., Amorim, A., Breitenlechner, M., Downard, A. J., Dunne, E. M., Flagan, R. C., Kajos,  
779 M., Keskinen, H., Kirkby, J., Kupc, A., Kürten, A., Kurtén, T., Laaksonen, A., Mathot, S., Onnela,  
780 A., Praplan, A. P., Rondo, L., Santos, F. D., Schallhart, S., Schnitzhofer, R., Sipilä, M., Tomé, A.,  
781 Tsagkogeorgas, G., Vehkamäki, H., Wimmer, D., Baltensperger, U., Carslaw, K. S., Curtius, J.,  
782 Hansel, A., Petäjä, T., Kulmala, M., Donahue, N. M., and Worsnop, D. R.: Molecular  
783 understanding of atmospheric particle formation from sulfuric acid and large oxidized organic  
784 molecules., *PNAS*, 110, 17223-17228, 2013.

785  
786 Shi, J. P., Evans, D. E., Khan, A. A., and Harrison, R. M.: Sources and concentration of  
787 nanoparticles (<10nm diameter) in the urban atmosphere, *Atmos. Environ.*, 35, 1193-1202, 2001.

788  
789 Shi, Z., Vu, T., Kotthaus, S., Harrison, R.M., Grimmond, S., Yue, S., Zhu, T., Lee, J., Han, Y.,  
790 Demuzere, M., Dunmore, R.E., Ren, L., Liu, D., Wang, Y., Wild, O., Allan, J., Acton, W.J.,  
791 Barlow, J., Barratt, B., Beddows, D., Bloss, W.J., Calzolari, G., Carruthers, D., Carslaw, D.C., Chan,  
792 Q., Chatzidiakou, L., Chen, Y., Crilley, L., Coe, H., Dai, T., Doherty, R., Duan, F., Fu, P., Ge, B.,  
793 Ge, M., Guan, D., Hamilton, J.F., He, K., Heal, M., Heard, D., Hewitt, C.N., Holloway, M., Hu, M.,  
794 Ji, X. Jiang, R. Jones, M. Kalberer, F.J. Kelly, L. Kramer, B. Langford, C. Lin, A.C. Lewis, J. Li,  
795 W. Li, D., Liu, H., Liu, J., Loh, M., Lu, K., Lucarelli, F., Mann, G., McFiggans, G., Miller, M.R.,  
796 Mills, G., Monk, P., Nemitz, E., O'Connor, F., Ouyang, B., Palmer, P.I., Percival, C., Popoola, O.,  
797 Reeves, C., Rickard, A.R., Shao, L., Shi, G., Spracklen, D., Stevenson, D., Sun, Y., Sun, Z., Tao, S.,  
798 Tong, S., Wang, Q., Wang, W., Wang, X., Wang, X., Wang, Z., Wei, L., Whalley, L., Wu, X., Wu,  
799 Z., Xie, P., Yang, F., Zhang, Q., Zhang, Y., Zhang, Y. and Zheng, M.: In-depth study of air  
800 pollution sources and processes within Beijing and its surrounding region (APHH-Beijing), *Atmos.*  
801 *Chem. Phys.*, 19, 7519-7546, 2019.

802  
803 Stolzenburg, D, Fischer, L., Vogel, A., Heinritzi, M., Schervish, M., Simon, M., Wagner, A.,  
804 Dada, L., Ahonen, L., Amorim, A., Baccharini, A., Bauer, P., Baumgartner, B., Bergen, A.,  
805 Bianchi, F., Breitenlechner, M., Brilke, S., Buenrostro Mazon, S., Chen, D., Dias, A., Draper, D.,  
806 Duplissy, J., El Haddad, I., Finkenzeller, H., Frege, C., Fuchs, C., Garmash, O., Gordon, H., He, X.,  
807 Helm, J., Hofbauer, V., Hoyle, C., Kim, C., Kirkby, J., Kontkanen, J., Kürten, A., Lampilahti, J.,  
808 Lawler, M., Lehtipalo, K., Leiminger, M., Mai, H., Mathot, S., Mentler, B., Molteni, U., Nie, W.,  
809 Nieminen, T., Nowak, J., Ojdanic, A., Onnela, A., Passananti, M., Petäjä, T., Quéléver, L.,  
810 Rissanen, M., Sarnela, N., Schallhart, S., Tauber, C., Tomé, A., Wagner, R., Wang, M., Weitz, L.,  
811 Wimmer, D., Xiao, M., Yan, C., Ye, P., Zha, Q., Baltensperger, U., Curtius, J., Dommen, J., Flagan,  
812 R., Kulmala, M., Smith, J., Worsnop, D., Hansel, A., Donahue, N., Winkler, P., Rapid growth of  
813 organic aerosol nanoparticles over a wide tropospheric temperature range, *PNAS*, 115, 9122-9127,  
814 2018.

815  
816 Tammet, H.: Size and mobility of nanometer particles, clusters and ions, *J. Aerosol Sci.*, 26, 459-  
817 475, 1995.

818  
819 Tomasi, C., Fuzzi, S., Kokhanovsky, A.: *Atmospheric Aerosols: Life Cycles and Effects on Air*  
820 *Quality and Climate*, Wiley, 2016.

821

822 Tröstl, J., Chuang, W. K., Gordon, H., Heinritzi, M., Yan, C., Molteni, U., Ahlm, L., Frege, C.,  
823 Bianchi, F., Wagner, R., Simon, M., Lehtipalo, K., Williamson, C., Craven, J. S., Duplissy, J.,  
824 Adamov, A., Almeida, J., Bernhammer, A. K., Breitenlechner, M., Brilke, S., Dias, A., Ehrhart, S.,  
825 Flagan, R. C., Franchin, A., Fuchs, C., Guida, R., Gysel, M., Hansel, A., Hoyle, C. R., Jokinen, T.,  
826 Junninen, H., Kangasluoma, J., Keskinen, H., Kim, J., Krapf, M., Kürten, A., Laaksonen, A.,  
827 Lawler, M., Leiminger, M., Mathot, S., Möhler, O., Nieminen, T., Onnela, A., Petäjä, T., Piel, F.  
828 M., Miettinen, P., Rissanen, M. P., Rondo, L., Sarnela, N., Schobesberger, S., Sengupta, K., Sipilä,  
829 M., Smith, J. N., Steiner, G., Tomè, A., Virtanen, A., Wagner, A. C., Weingartner, E., Wimmer, D.,  
830 Winkler, P. M., Ye, P., Carslaw, K. S., Curtius, J., Dommen, J., Kirkby, J., Kulmala, M., Riipinen,  
831 I., Worsnop, D. R., Donahue, N. M., and Baltensperger, U.: The role of low-volatility organic  
832 compounds in initial particle growth in the atmosphere, *Nature*, 533, 527-531,  
833 <https://doi.org/10.1038/nature18271>, 2016.

834  
835 Wang, S., Wu, R., Berndt, T., Ehn, M., and Wang, L.: Formation of Highly Oxidized Radicals and  
836 Multifunctional Products from the Atmospheric Oxidation of Alkylbenzenes, *Environ. Sci. Techn.*,  
837 51, 8442-8449, 2017.

838  
839 Wang, Z., Wu, Z., Yue, D., Shang, D., Guo, S., Sun, J., Ding, A., Wang, L., Jiang, J., Guo, H., Gao,  
840 J., Cheung, H. C., Morawska, L., Keywood, M., and Hu, M.: New particle formation in China:  
841 Current knowledge and further directions, *Sci. Tot. Environ.*, 577, 258-266, 2016.

842  
843 Wiedensohler, A., Cheng, Y. F., Nowak, A., Wehner, B., Achtert, P., Berghof, M., Birmili, W., Wu,  
844 Z. J., Hu, M., Zhu, T., Takegawa, N., Kita, K., Kondo, Y., Lou, S. R., Hofeumahaas, A., Holland,  
845 F., Wahner, A., Gunthe, S. S., Rose, D., Su, H., and Pöschl, U.: Rapid aerosol particle growth and  
846 increase of cloud condensation nucleus activity by secondary aerosol formation and condensation:  
847 A case study for regional air pollution in northeastern China, *Journal of Geophysical Research*  
848 *Atmospheres*, 114, 1–13, <https://doi.org/10.1029/2008JD010884>, 2009.

849  
850 Wu, Z., Hu, M., Lin, P., Liu, S., Wehner, B., and Wiedensohler, A.: Particle number size  
851 distribution in the urban atmosphere of Beijing, China, *Atmos. Environ.*, 42, 7967-7980, 2008.

852  
853 Wu, Z., Ma, N., Größ, J., Kecorius, S., Lu, K., Shang, D., Wang, Y., Wu, Y., Zeng, L., Hu, M.,  
854 Wiedensohler, A., and Zhang, Y.: Thermodynamic properties of nanoparticles during new particle  
855 formation events in the atmosphere of North China Plain, *Atmos. Res.*, 188, 55-63, 2017.

856  
857 Wu, Z. J., Hu, M., Liu, S., Wehner, B., Bauer, S., Ssling, a. M., Wiedensohler, a., Petäjä, T., Dal  
858 Maso, M., and Kulmala, M.: New particle formation in Beijing, China: Statistical analysis of a 1-  
859 year data set, *J. Geophys. Res. Atmospheres*, 112, D09209, <https://doi.org/10.1029/2006JD007406>,  
860 2007.

861  
862 Xiong, F., McAvey, K. M., Pratt, K. A., Groff, C. J., Hostetler, M. A., Lipton, M. A., Starn, T. K.,  
863 Seeley, J. V., Bertman, S. B., Teng, A. P., Crouse, J. D., Nguyen, T. B., Wennberg, P. O., Misztal,  
864 P. K., Goldstein, A. H., Guenther, A. B., Koss, A. R., Olson, K. F., De Gouw, J. A., Baumann, K.,  
865 Edgerton, E. S., Feiner, P. A., Zhang, L., Miller, D. O., Brune, W. H., and Shepson, P. B.:  
866 Observation of isoprene hydroxynitrates in the Southeastern United States and implications for the  
867 fate of NO<sub>x</sub>, *Atmos. Chem. Phys.*, 15, 11257-11272, 2015 .

868  
869 Yan, C., Nie, W., Äijälä, M., Rissanen, M. P., Canagaratna, M. R., Massoli, P., Junninen, H.,  
870 Jokinen, T., Sarnela, N., Häme, S. A. K., Schobesberger, S., Canonaco, F., Yao, L., Prévôt, A. S.  
871 H., Petäjä, T., Kulmala, M., Sipilä, M., Worsnop, D. R., and Ehn, M.: Source characterization of  
872 highly oxidized multifunctional compounds in a boreal forest environment using positive matrix  
873 factorization, *Atmos. Chem. Phys.*, 16, 12715-12731, 2016.

874 Yao, L., Garmash, O., Bianchi, F., Zheng, J., Yan, C., Kontkanen, J., Junninen, H., Mazon, S. B.,  
875 Ehn, M., Paasonen, P., Sipilä, M., Wang, M., Wang, X., Xiao, S., Chen, H., Lu, Y., Zhang, B.,  
876 Wang, D., Fu, Q., Geng, F., Li, L., Wang, H., Qiao, L., Yang, X., Chen, J., Kerminen,  
877 V. M., Petäjä, T., Worsnop, D. R., Kulmala, M., and Wang, L.: Atmospheric new particle formation  
878 from sulfuric acid and amines in a Chinese megacity, *Science*, 361, 278-281, 2018.  
879  
880 Yu, F. and Luo, G.: Simulation of particle size distribution with a global aerosol model:  
881 Contribution of nucleation to aerosol and CCN number concentrations, *Atmospheric Chemistry and*  
882 *Physics*, 9, 7691-7710, 2009.  
883  
884 Yue, D. L., Hu, M., Zhang, R. Y., Wu, Z. J., Su, H., Wang, Z. B., Peng, J. F., He, L. Y., Huang, X.  
885 F., Gong, Y. G., and Wiedensohler, A.: Potential contribution of new particle formation to cloud  
886 condensation nuclei in Beijing, *Atmos. Environ.*, 45, 6070-6077, 2011.  
887  
888 Zhao, Y., Wingen, L. M., Perraud, V., Greaves, J., and Finlayson-Pitts, B. J.: Role of the reaction of  
889 stabilized Criegee intermediates with peroxy radicals in particle formation and growth in air, *Phys.*  
890 *Chem. Chem. Phys.*, 17, 12500-12514, 2015.  
891

892 **FIGURE LEGENDS:**

893

894 **Figure 1** Oxidation state of carbon calculated as two times the oxygen to carbon ratio minus the  
895 hydrogen to carbon ratio against carbon number for (colored) individual ions and (blue  
896 circles) signal weighted average for each carbon number. Area and colour are both  
897 proportional to the peak area for each ion  
898

899 **Figure 2** Mass defect plot of fitted mass spectral peaks between 100-600mass units on (a) 10:30  
900 – 12:00 23/06/2017, a non nucleation day, and (b) 10:30 -12:00 25/06/2017, a  
901 nucleation day. Mass defect can be defined as the mass - integer mass. The size of point  
902 is proportional to the signal intensity. As  $^1\text{H}$  has a positive mass defect (1.007276 Da),  
903 the upward trend along the horizontal indicates increasing carbon chain length, and  
904 differences at similar masses are due to increasing oxygen functionality, clustering with  
905 species such as sulfuric acid (negative mass defect) and ammonia (positive mass  
906 defect), as  $^{16}\text{O}$  and  $^{32}\text{S}$  have negative mass defects (15.9949 and 31.9721 Da  
907 respectively), while  $^{14}\text{N}$  has a positive mass defect at 14.0031 Da.  
908

909 **Figure 3** Summed time series of the concentrations of (A) all non-nitrogen containing HOMs and  
910 all organonitrates identified, (B) C5, C10 and C20 components, assumed to be  
911 dominated by isoprene, monoterpene monomer and monoterpene dimers, signal for C20  
912 multiplied 50 times to fit scale, and (C) summed C6 - C9 components, and summed C11  
913 - C18 components, assumed to be dominated by alkylbenzenes and other larger  
914 components respectively.  
915

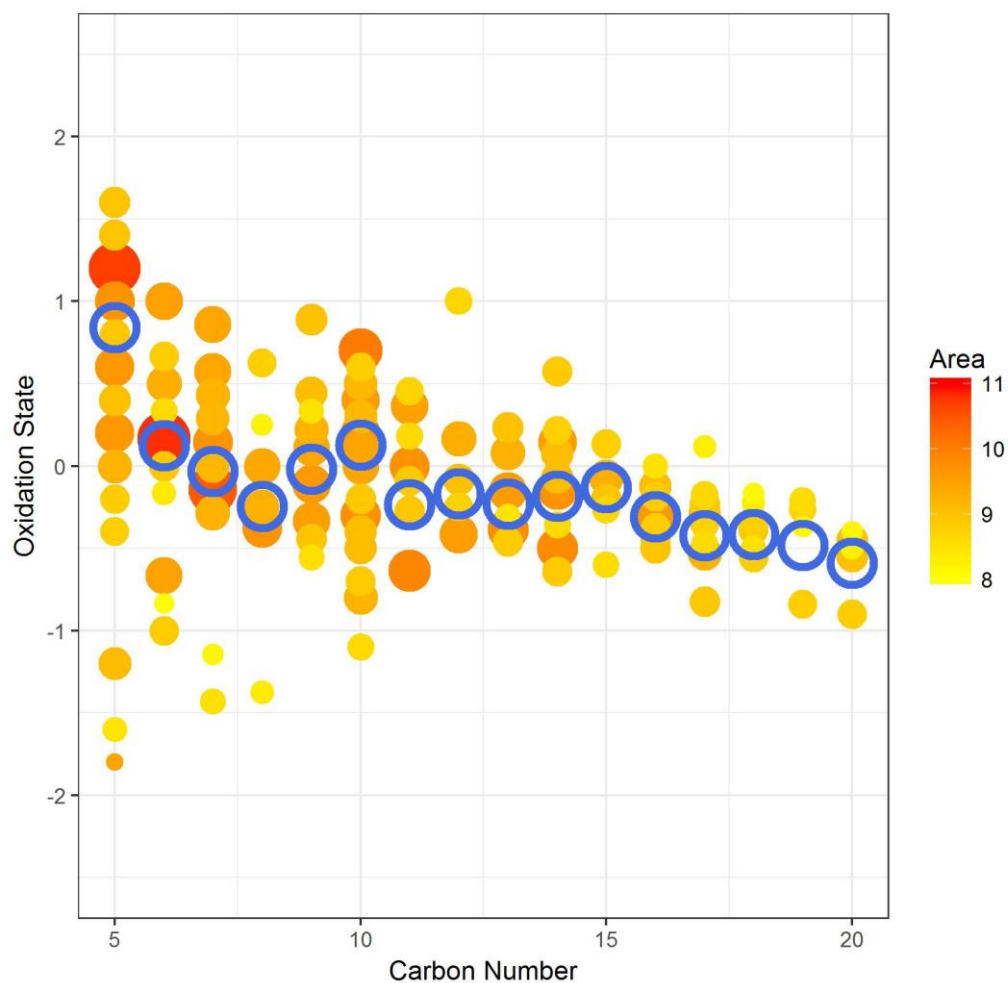
916 **Figure 4** Time series for the whole sampling campaign for the concentrations of (left axis) VOCs  
917 as measured by PTR-ToF and (right axis) a selected HOM product associated with that  
918 precursor.  
919

920 **Figure 5** Normalised unit mass  $\text{NO}_3$ - CI-APi-ToF signal intensity on 24/06/2017 (A) and  
921 25/06/2017 (B). Each individual unit mass was normalised to a maximum of 1. Each  
922 period is normalised separately so the individual signal maxima on each day are visible.  
923 The graph is plotted between 200-600 mass units, with every 10 mass units averaged for  
924 simplicity. On the secondary axis is plotted PSM data, both total particle count  $>1.30$   
925 nm (black trace) and total clusters between 1.30 and 1.84 nm (blue trace). Data is  
926 plotted at 1 hour time resolution.  
927

928 **Figure 6** SMPS + PSM contour plot for two nucleation days on 24/06/2017 and 25/06/2017. Data  
929 in bottom panel is from the PSM instrument, top panel from NanoSMPS, units in colour  
930 bar are  $\log_{10}(\text{dN}/\log D_p)$  for N in  $\text{cm}^{-3}$ . Points signify normalised sulfuric acid  
931 concentration (right axis) as measured by CI-APi-ToF.  
932

933

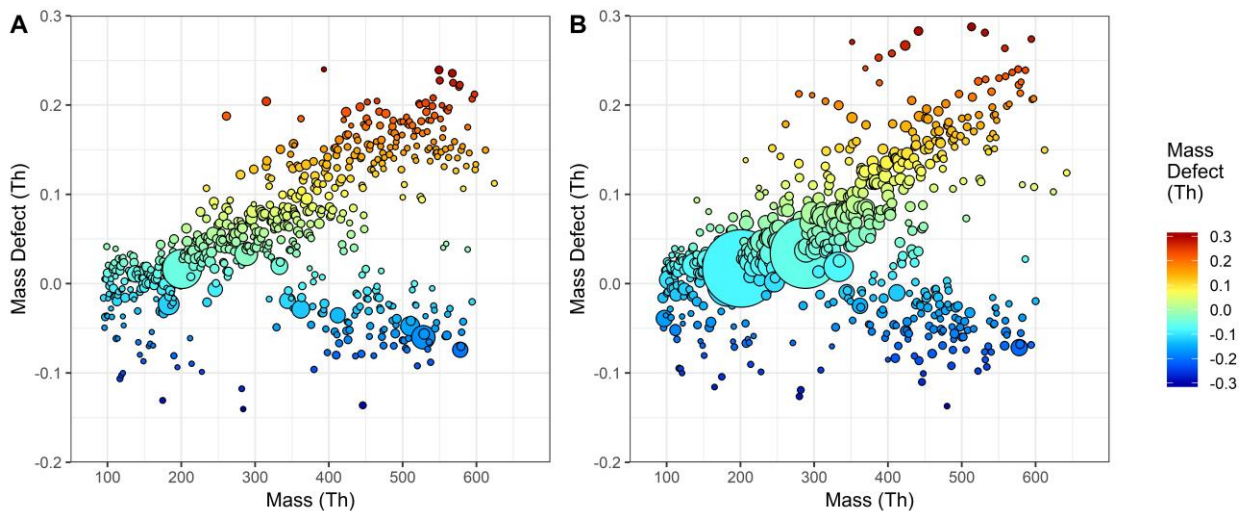
934



935

936 **Figure 1.** Oxidation state of carbon plotted against carbon number for (colored) individual ions and  
937 (blue circles) signal weighted average for each carbon number. Area and colour are both proportional  
938 to the peak area for each ion.

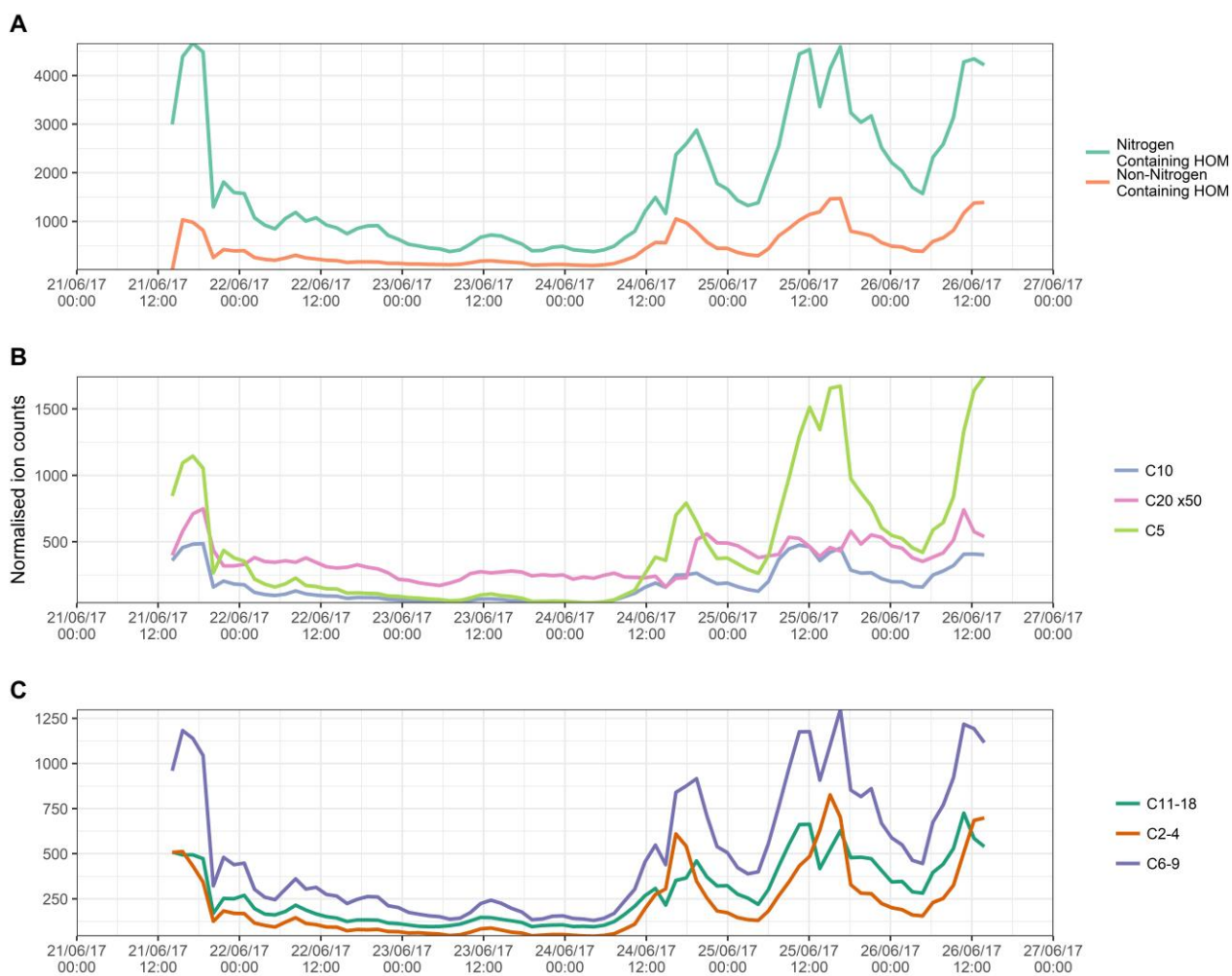
939



941

942 **Figure 2.** Mass defect plot of fitted mass spectral peaks between 100-600mass units on (a) 10:30 –  
 943 12:00 23/06/2017, a non nucleation day, and (b) 10:30 -12:00 25/06/2017, a nucleation day. Mass  
 944 defect can be defined as the mass - integer mass. The size of point is proportional to the signal  
 945 intensity. As  $^1\text{H}$  has a positive mass defect (1.007276 Da), the upward trend along the horizontal  
 946 indicates increasing carbon chain length, and differences at similar masses are due to increasing  
 947 oxygen functionality, clustering with species such as sulfuric acid (negative mass defect) and  
 948 ammonia (positive mass defect), as  $^{16}\text{O}$  and  $^{32}\text{S}$  have negative mass defects (15.9949 and 31.9721 Da  
 949 respectively), while  $^{14}\text{N}$  has a positive mass defect at 14.0031 Da.

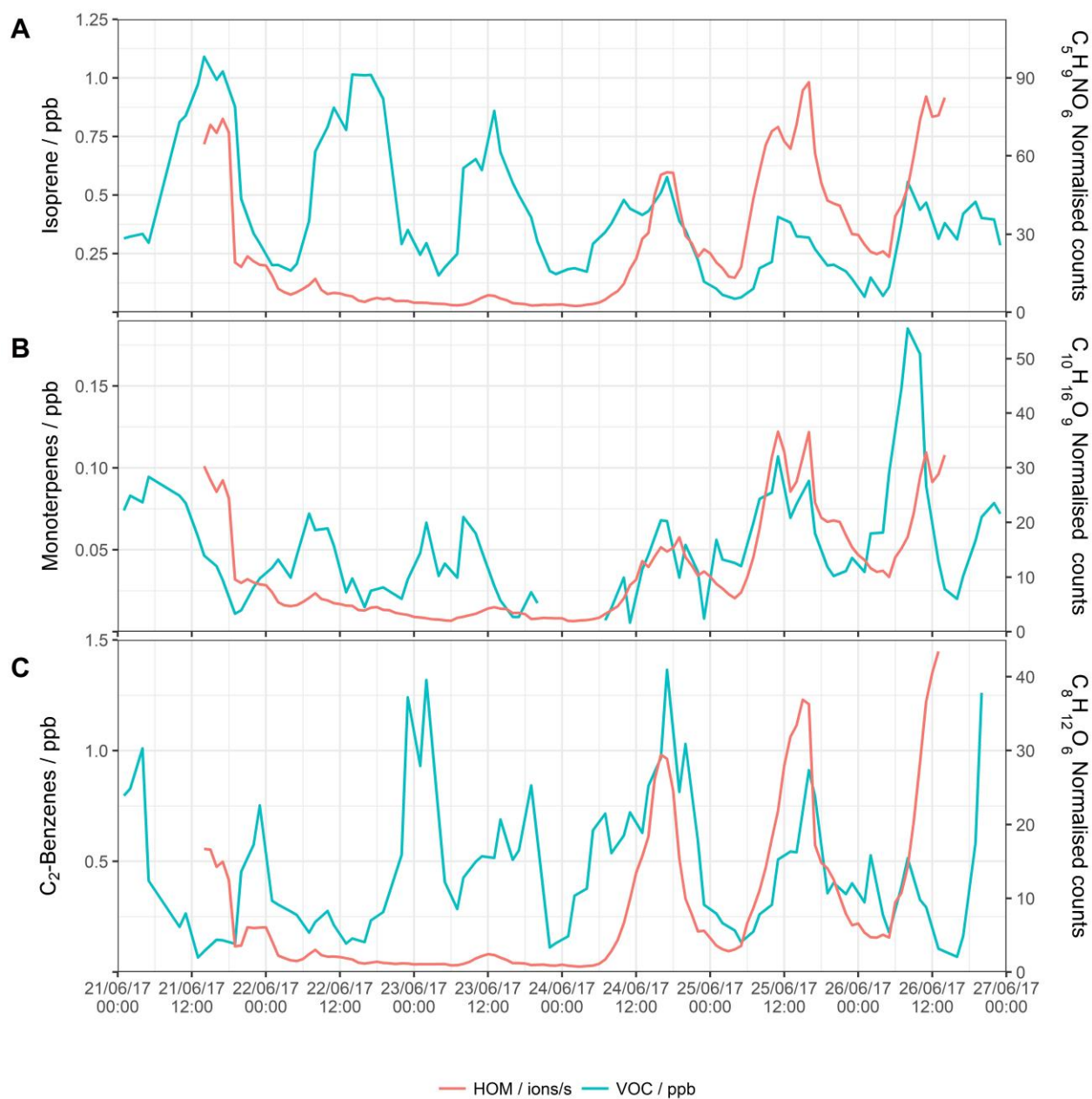
950



951

952 **Figure 3.** Summed time series of the concentrations of (A) all non-nitrogen containing HOMs and  
 953 all organonitrates identified, (B) C5, C10 and C20 components, assumed to be dominated by isoprene,  
 954 monoterpene monomer and monoterpene dimers, signal for C20 multiplied 50 times to fit scale, and  
 955 (C) summed C6 - C9 components, and summed C11 - C18 components, assumed to be dominated by  
 956 alkylbenzenes and other larger components respectively.





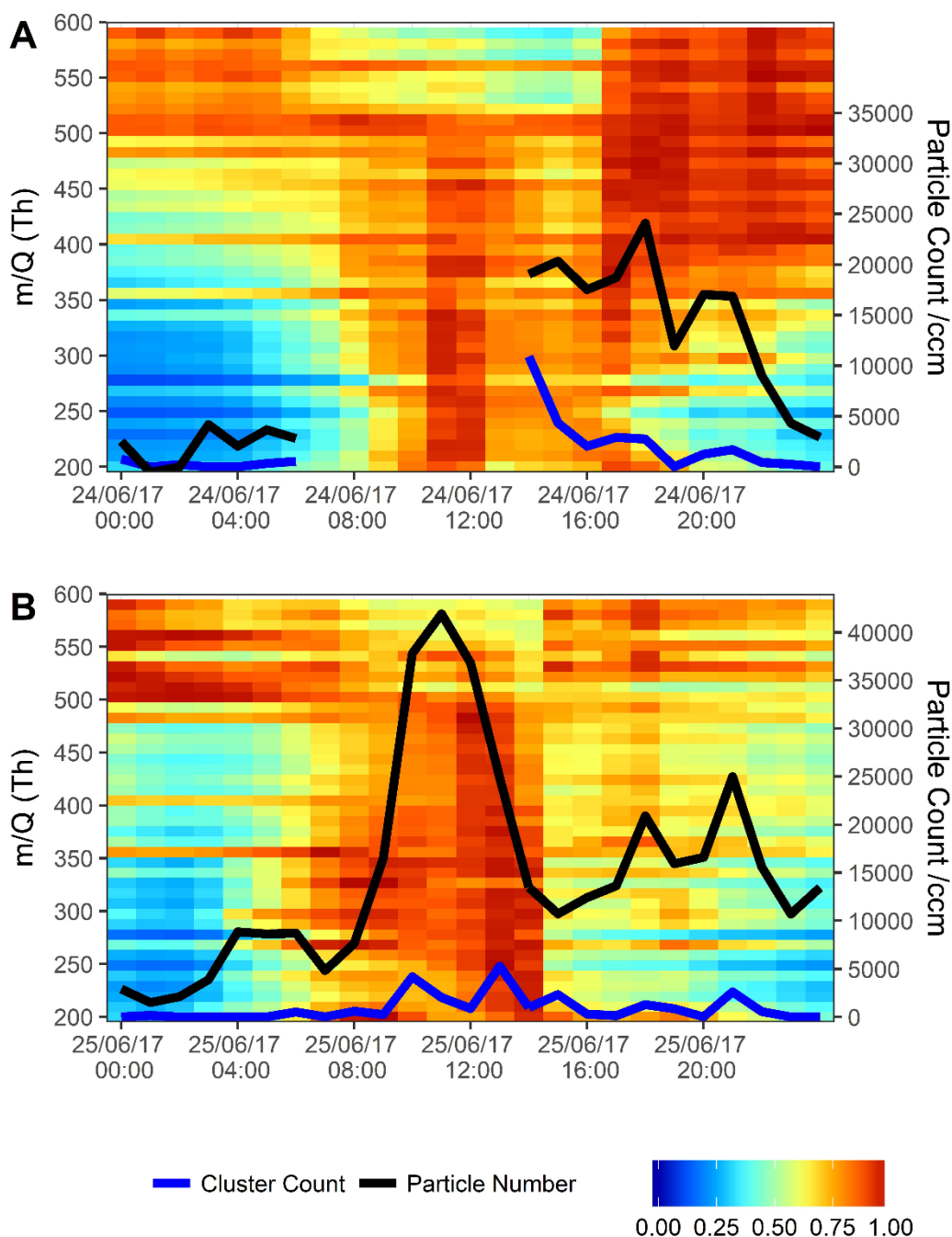
957

958 **Figure 4.** Time series for the whole sampling campaign for the concentrations of (left axis) VOCs as  
 959 measured by PTR-ToF and (right axis) a selected HOM product associated with that precursor.

960

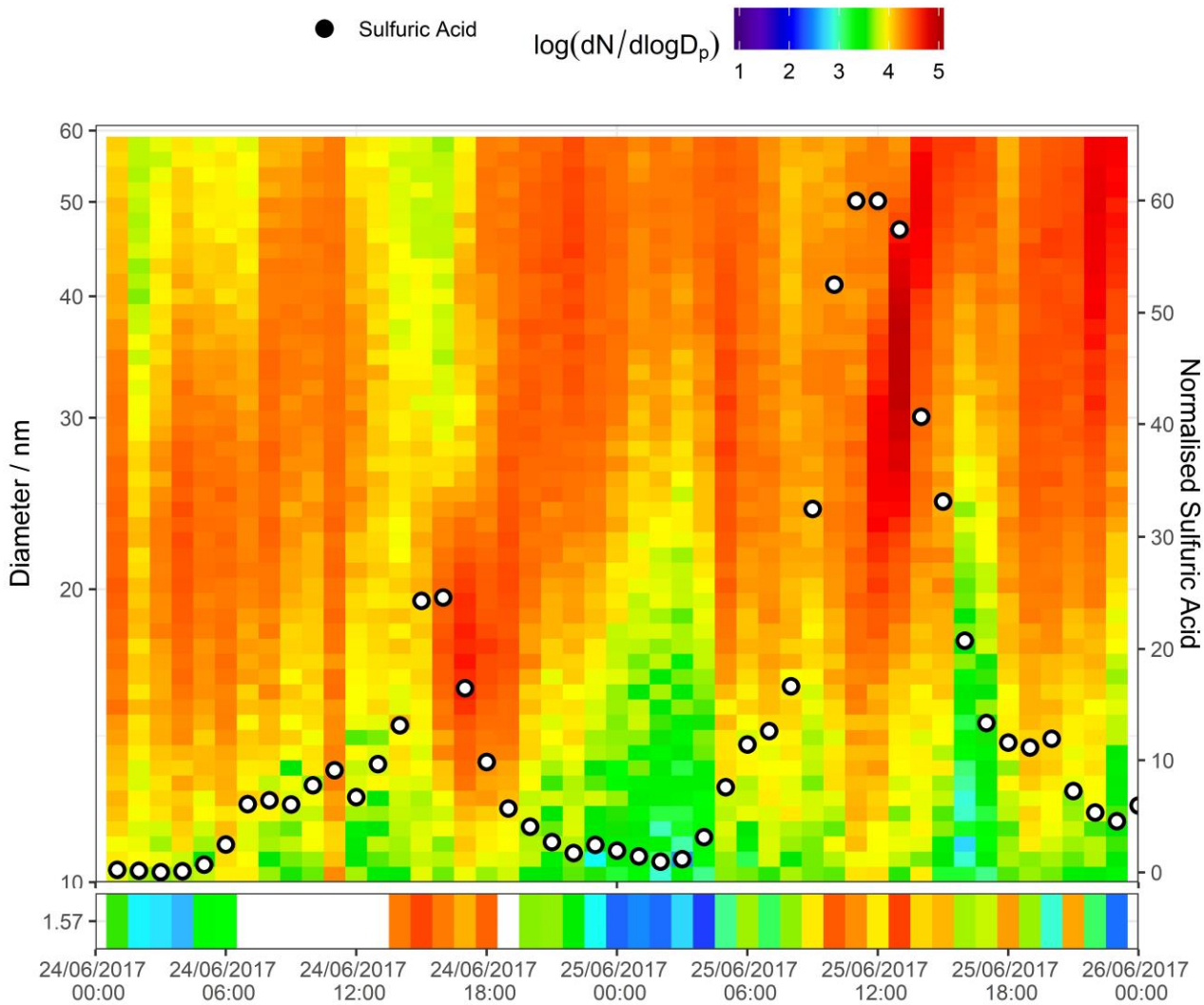
961

962



963

964 **Figure 5.** Normalised unit mass  $\text{NO}_3^-$  CI-APi-ToF signal intensity on 24/06/2017 (A) and 25/06/2017  
 965 (B). Each individual unit mass was normalised to a maximum of 1. Each period is normalised  
 966 separately so the individual signal maxima on each day are visible. The graph is plotted between 200-  
 967 600 mass units, with every 10 mass units averaged for simplicity. On the secondary axis is plotted  
 968 PSM data, both total particle count  $>1.30$  nm (black trace) and total clusters between 1.30 and 1.84  
 969 nm (blue trace). Data is plotted at 1 hour time resolution.



970

971 **Figure 6.** SMPS + PSM contour plot for two nucleation days on 24/06/2017 and 25/06/2017. Data in  
 972 bottom panel is from the PSM instrument, top panel from NanoSMPS, units in colour bar are  $\log_{10}$   
 973  $(dN/\log D_p)$  for  $N$  in  $\text{cm}^{-3}$ . Points signify normalised sulfuric acid concentration (right axis) as  
 974 measured by CI-APi-ToF.

975

976

977

978

979

980

981